


Pair density wave and loop current promoted by Van Hove singularities in moiré systems

Zhengzhi Wu ¹, Yi-Ming Wu,¹ and Fengcheng Wu ^{2,3}

¹*Institute for Advanced Study, Tsinghua University, Beijing 100084, China*

²*School of Physics and Technology, Wuhan University, Wuhan 430206, China*

³*Wuhan Institute of Quantum Technology, Wuhan 430206, China*

 (Received 23 July 2022; revised 27 October 2022; accepted 3 January 2023; published 17 January 2023)

We theoretically show that in the presence of conventional or higher order Van Hove singularities (VHS), the bare finite momentum pairing, also known as the pair density wave (PDW), susceptibility can be promoted to the same order of the most divergent bare BCS susceptibility through a valley-contrasting flux 3ϕ in each triangular plaquette at $\phi = \pi/3$ and $\pi/6$ in moiré systems. This makes the PDW order a possible leading instability for an electronic system with repulsive interactions. We confirm that it indeed wins over all other instabilities and becomes the ground state under certain conditions through the renormalization group calculation and a flux insertion argument. Moreover, we also find that a topological nontrivial loop current order becomes the leading instability if the Fermi surface with conventional VHS is perfectly nested at $\phi = \pi/3$. Similar to the Haldane model, this loop current state has the quantum anomalous Hall effect. If we dope this loop current state or introduce a finite next-nearest-neighbor hopping t' , the chiral d -wave PDW becomes the dominant instability. Experimentally, the flux can be effectively tuned by an out-of-plane electric field in moiré systems based on graphene and transition metal dichalcogenides.

DOI: [10.1103/PhysRevB.107.045122](https://doi.org/10.1103/PhysRevB.107.045122)

I. INTRODUCTION

Although superconductivity from the condensation of zero center-of-mass momentum Cooper pairs is commonly observed in many superconducting materials, that with finite momentum Cooper pairs, also known as pair density wave (PDW), stays rare in nature [1]. The PDW can be thought as a superconducting state with periodic spatial modulations in the order parameter, which vanishes on average. Its rareness can be ascribed to the fact that, for a conventional Fermi liquid with time-reversal and inversion symmetry, the pairing susceptibility $\chi_{sc}(\mathbf{q}, T)$ diverges only at $\mathbf{q} = 0$ in low-energy limit. The first proposal for the finite \mathbf{q} pairing is the Fulde-Ferrell-Larkin-Ovchinnikov (FFLO) state [2,3], which is predicted to exist in a clean superconductor in the presence of a high magnetic field if the orbital pairing breaking effect is negligible, i.e., without the creation of Abrikosov vortices, and the superconducting state persists up to the Pauli limit. So stringent are these conditions that very few materials can realize this FFLO state. Nonetheless, some experimental evidence for its existence have been reported in organic superconductors [4], heavy fermion compounds [5], and iron-based superconductors [6,7].

In underdoped cuprates, the PDW has been proposed as a competitor to d -wave uniform superconductivity [8–11]. Unlike the FFLO state, this PDW has zero coupling to the external magnetic field, and arises from strong electronic correlation. As a result, it coexists or neighbors with other charge or spin orders in the phase diagram [12–14]. The complicated interplay among PDW and other electronic orders makes it hard to identify which order is primary. Because of

this complicated interplay, another scenario is also proposed, where the PDW is argued to be the mother order, while other orders are descendants from it [15,16]. Indeed, through partial melting of a PDW, there may be other vestigial orders such as charge density wave or nematicity, appearing through a cascade of finite T transitions [17–19]. Probably the most nontrivial result from this scenario is the development of the highly exotic charge- $4e$ or even charge- $6e$ superconductors [20,21], of which the experimental signatures have not been reported until very recently [22]. With these many unsettled yet interesting puzzles, it is highly valuable to find a platform which can realize the PDW order as a unique ground state, and the interplay between different orders at finite temperature can be investigated in depth.

Here in this paper, we argue that a certain class of two-dimensional moiré band structures with either conventional [23–25] or higher order [26–29] Van Hove singularities (VHS) can serve as the promising platform for hosting the PDW in the ground state. A Van Hove singularity occurs in a two-dimensional system when the Fermi level is tuned to the energy dispersion saddle point where $\nabla_{\mathbf{k}}\epsilon(\mathbf{k}) = 0$. Formally, we can distinguish two different VHS's using the 2×2 Hessian matrix defined by $D_{ij} = 1/2\partial_{k_i}\partial_{k_j}\epsilon(\mathbf{k})$. The conventional Van Hove singularity (CVHS) is the one with $\det D < 0$, e.g., $\epsilon(\mathbf{k}) = k_x^2 - k_y^2$; while for the higher order Van Hove singularity (HOVHS) we have $\det D = 0$. Examples of HOVHS include $\epsilon(\mathbf{k}) = k_y^2 - k_x^4$ and $\epsilon(\mathbf{k}) = k_x(k_x^2 - \sqrt{3}k_y^2)$, and we will focus on the second type in this paper. The interesting feature about VHS is that the fermion density of states diverges at this particular filling, and more often than not, the VHS is associated with Fermi surface nesting. These facts indicate

that there has to be a competition among different electronic orders, in both particle-hole channel and particle-particle channel. There have been plenty of discussions of competing orders near the CVHS in the literature [30–37]. However, even with nested Fermi surface, it is various particle-hole density wave orders, such as charge density wave and spin density wave orders, that generally win over uniform superconducting orders in the previous studies, and in the perfectly nested case, particle hole condensate wins over superconductivity [30,32,33] as the nesting enhances the bare particle-hole susceptibility $\Pi_{ph}(\mathbf{Q}, T)$ at finite momentum as the same order as the bare particle-particle susceptibility $\Pi_{pp}(0, T)$, which scales as $\ln^2(W/T)$ with W being the bandwidth. Nevertheless, it is very rare that the bare $\Pi_{pp}(\mathbf{Q}, T)$ can be enhanced to the same order of $\Pi_{pp}(0, T)$, which is a necessary condition for the PDW order to be the leading instability in the weak coupling regime. For the HOVHS case, all the bare susceptibilities diverge in a power-law manner, because the power-law divergence of the density of states. This naturally promotes the bare PDW susceptibility, but PDW still needs to compete with other orders. In this work, we show that by tuning the effective valley-dependent flux in the moiré system, which can be controlled, for example, by an applied out-of-plane displacement field, the system at either CVHS and HOVHS can favor the stable PDW order as the ground state with repulsive interactions.

The model we use is inspired by the moiré band structure of the twisted bilayer transition metal dichalcogenides (TMD) [38–49], the ABC stacked trilayer graphene on h-BN [50–52], twisted double bilayer graphene [27,53–58], and also twisted bilayer graphene [32,59–62]. In all these systems, the small twist angle or the small lattice constant mismatch results in a large scale triangular moiré pattern. The moiré superlattices profoundly change the low-energy band structure, and in some cases lead to nearly flat band, where the interaction plays an important role. Therefore these systems have been suggested to simulate the Hubbard physics [38]. Apart from the twist angle, a valley-contrasting flux is another important tuning parameter in these systems. This flux changes the noninteracting band structure dramatically. For example, it changes the location of the Van Hove singularities and the Fermi surface nesting in both the particle-particle and particle-hole channels, and thus controls the bare susceptibilities of various orders. This flux can be modeled by endowing the nearest-neighbor hopping t with a complex phase factor ϕ and modifying t into $te^{i\phi}$. Experimentally, the valley-contrasting flux can be effectively tuned by an out-of-plane electric field [63–66].

In Fig. 1, we show how the Fermi surfaces with only nearest-neighbor hopping for different valleys evolve with different ϕ . For the realistic system, the next-nearest-neighbor hopping t' should also be considered, as it reduces the Fermi surface nesting and suppresses the particle-hole channel density waves. We will discuss this point below. In the perfect nesting model with $\phi = 0$, electronic bands from different valleys can hardly be distinguished. In the ideal case, the valley components, together with the spin components, form four fermion flavors, giving rise to an (emergent) SU(4) symmetry in the noninteracting Hamiltonian. A nonzero ϕ breaks this symmetry and also spoils some degeneracy which is protected by the SU(4) symmetry. We show that there is a symmetry

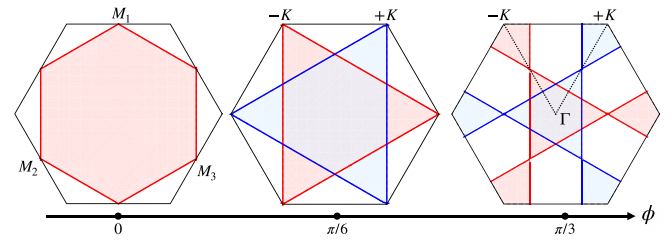


FIG. 1. Perfectly nested low-energy Fermi surfaces of moiré systems for different valleys (red and blue lines) in the presence of a valley-contrasting flux. In the absence of the flux, Van Hove singularity appears when the system is doped to the M point. As ϕ increases, there can be two higher order Van Hove singularities located at the Brillouin zone corners, or six conventional Van Hove singularities at the middle point between Γ (Brillouin zone center) and $\pm K$.

transformation regarding ϕ , which turns the valley-polarized pairing at $\phi = 0$ to a PDW order at $\phi = \pi/3$, for which there are six CVHS in the moiré Brillouin zone at Van Hove doping. The case with $\phi = \pi/6$ is of special interest because there are two HOVHS points located at the moiré Brillouin zone corners $\pm K$.

To investigate the competing orders and obtain the phase diagram in an unbiased way, we thereby employ the parquet renormalization group (pRG) analysis. This was first introduced in the discussion of meson scattering [67] and was later successfully applied to discuss competing orders in interacting one-dimensional electron gas [68], cuprates [30,69], iron-based superconductors [70], graphene [31], and more recently, moiré band structures with Van Hove fermiology [33–35]. It involves in identifying the leading divergent free susceptibilities, and inserting them as building blocks to renormalize different interactions, which helps to identify the leading instability in the low-energy limit. Based on the noninteracting band structure, we further introduce different initial interactions as the input of our RG analysis.

Our results are obtained for the CVHS and HOVHS separately. In the conventional case with $\phi = \pi/3$ and SU(4) preserving interactions, we find that PDW loses to a topological loop current order in the perfect nesting limit, i.e., with a vanishing t' and the filling fraction approaching the Van Hove filling. This loop current order results from an imaginary d -wave particle-hole condensate, and is similar to the Haldane model for quantum anomalous Hall effect [71]. This loop current has been previously discussed in the context of a $\phi \rightarrow 0$ model with the fermion flavor equal to 4. We show that indeed in our model, the loop current order at $\phi = \pi/3$ is related to that at $\phi = 0$ via a symmetry transformation. When the system is tuned away from the perfect nesting, we find that the ground state favors a chiral d -wave PDW instead. If we include SU(4) breaking interactions, such as Hund coupling, the chiral- d wave or s -wave PDW exists in a wide parameter space as a stable phase even in the perfect nesting limit. Again, via symmetry transformation, this PDW is related to the chiral d -wave valley-polarized uniform superconductivity at $\phi = 0$. As a result, PDW phase can also exist for a generic filling $\nu = n$ (ν is the number of electrons per site) at $\phi = \pi/3$ (although not necessarily the chiral d -wave PDW), as long

as the same interactions favor the valley polarized uniform superconductivity at $\phi = 0$ and filling $\nu = 4 - n$. For the higher order VHS, our results suggest that PDW can be the leading instability once a valley splitting field is introduced. The resulting PDW phase has a relatively high transition temperature and is thus more promising to be observed experimentally.

The paper is organized as following. In Sec. II, we introduce the lattice model inspired by the moiré band structure of twisted bilayer TMD, which is also relevant to the twisted double bilayer graphene system and ABC stacked trilayer graphene system. In Sec. III, we discuss the symmetries of our model and symmetry classification of the superconducting orders. In Sec. IV, we first introduce a flux insertion operation to connect the orders between $\phi = 0$ and $\pi/3$, which generates the ground state at $\phi = \pi/3$ from a corresponding result at $\phi = 0$. After that, we perform the concrete RG analysis for the conventional VHS, and the results are consistent with those obtained via the flux insertion operation from previous analysis. In Sec. V, we conduct the parquet RG analysis for the higher order Van Hove singularities of two patch model and one patch model, and find prevailing PDW order in the latter. Concluding remarks are presented in Sec. VI.

II. THE LATTICE MODEL

We consider the following triangular lattice model $\hat{H} = \hat{H}_0 + \hat{H}_I$, where the single particle Hamiltonian \hat{H}_0 is given by

$$\begin{aligned} \hat{H}_0 = & -t \sum_i \sum_{v=\pm, f} e^{iv\phi} \hat{c}_{v,f}^\dagger(i) \hat{c}_{v,f}(i + \hat{a}_j) \\ & -t' \sum_{\langle\langle ij \rangle\rangle} \sum_{v=\pm, f} \hat{c}_{v,f}^\dagger(i) \hat{c}_{v,f}(j) + \text{H.c.}, \end{aligned} \quad (1)$$

where t and t' are the nearest-neighbour and next-nearest-neighbor hopping amplitudes. $\hat{a}_j = \hat{a}_1, \hat{a}_2, \hat{a}_3$ are the three nearest-neighbour unit vectors on the triangular lattice (with lattice constant $a = 1$): $\hat{a}_1 = (1, 0)$, $\hat{a}_2 = (-1/2, \frac{\sqrt{3}}{2})$, $\hat{a}_3 = (-1/2, -\frac{\sqrt{3}}{2})$. $f = 1, 2, \dots, N_f$ is the fermion flavor. This model describes spinless or spinful fermions (for each fixed v), where N_f is equal to one or two. A larger N_f can effectively describe multi-orbital physics. The most interesting part is the phase factor ϕ , which induces a flux $\pm 3\phi$ in each elementary triangle plaquette, and the flux is opposite for different valleys: $v = \pm$ represents the valley degree of freedom (DOF). This nontrivial flux pattern can be experimentally realized in the twisted homobilayer TMD (corresponding to $N_f = 1$) [66], twisted ABC trilayer graphene/h-BN, and twisted double bilayer graphene (corresponding to $N_f = 2$) [51]. The role of ϕ is to move the location of Van Hove singularities in the Brillouin zone. When $\phi = \pi/6$ and $t' = 0$, three Van Hove singularities within the same valley will merge into a higher-order Van Hove singularity.

The interacting Hamiltonian \hat{H}_I can be any symmetry-allowed four fermion interactions, including the Hubbard interaction, Heisenberg interaction, Hund interaction, etc. Ex-

plicitly \hat{H}_I with $N_f = 2$ can be written as

$$\begin{aligned} \hat{H}_I = & \frac{U}{2} \sum_i n_i^2 + J \sum_{\langle ij \rangle, n} c_i^\dagger T^n c_i c_j^\dagger T^n c_j \\ & + V_h \sum_i (c_i^\dagger \vec{S} c_i)^2 + K \sum_i (c_i^\dagger \vec{L} c_i)^2, \end{aligned} \quad (2)$$

where T^n are the fifteen generators of the SU(4) group, and J is the coupling constant of the Heisenberg interaction. The V_h and K are the coupling constants of spin and orbital Hund couplings, and $\vec{S} = \vec{\sigma}$, $\vec{L} = \vec{\tau}$ are the spin-1/2 Pauli matrices acting on the spin and valley degrees of freedom, respectively.

III. CLASSIFICATION OF ORDERS

In this section, we classify all the possible particle-hole and particle-particle orders which spontaneously break the global symmetries of Eq. (1). We will focus on $N_f = 2$, $\phi = \pi/3$, or $\phi = \pi/6$. Besides the $U(1)_c$ symmetry corresponding to the charge conservation and the lattice translation symmetry, the global symmetries of the lattice model is $SU(2)_s \times U(1)_v \times C_{3v}$, where $SU(2)_s$ is the spin rotation symmetry; $U(1)_v$ is the $U(1)$ valley (v) rotation symmetry, and C_{3v} is the point symmetry group of the lattice model.

We note that if $\phi = 0$ and $N_f = 2$, the lattice model Eq. (1) enjoys the SU(4) symmetry. Therefore we start with the spontaneous symmetry breaking of SU(4) symmetry, and then break this symmetry down to $SU(2)_s \times U(1)_v$ with a nonzero ϕ . The fermions c_f serve as the fundamental representation of the SU(4) internal symmetry. We physically view the four flavors which form the fundamental representation as spin 1/2 and valley pseudospin $\frac{1}{2}$ DOF. The tensor product of two fundamental representations of SU(4) group satisfies: $\mathbf{4} \otimes \mathbf{4} = \mathbf{6} \oplus \mathbf{10}$, $\bar{\mathbf{4}} \otimes \mathbf{4} = \mathbf{1} \oplus \mathbf{15}$, where $\mathbf{4}$ is the fundamental representation and $\bar{\mathbf{4}}$ is the complex conjugation of $\mathbf{4}$; $\mathbf{6}$ is the vector representation of SO(6) and $\mathbf{10}$ is the antisymmetric tensor representation of SO(6) [72]. The decomposition of $\mathbf{4} \otimes \mathbf{4} = \mathbf{6} \oplus \mathbf{10}$ means that the superconducting orders which spontaneously break the internal SU(4) symmetry can only be degenerate between spin-singlet-valley-triplet (ST) and spin-triplet-valley-singlet (TS), corresponding to the vector representation $\mathbf{6}$ [52,73]; or between spin-singlet-valley-singlet (SS) and spin-triplet-valley-triplet (TT), corresponding to the tensor representation $\mathbf{10}$ [52]. The vector representation $\mathbf{6}$ is parity even while the tensor representation $\mathbf{10}$ is parity odd. These superconducting orders include uniform superconductors and PDW orders, which may further break the C_{3v} and translational symmetry. Meanwhile, the decomposition $\bar{\mathbf{4}} \otimes \mathbf{4} = \mathbf{1} \oplus \mathbf{15}$ constraints the particle-hole orders. If the translation symmetry is broken, the identity representation $\mathbf{1}$ means the charge density wave order (CDW), and the representation $\mathbf{15}$ represents the degenerate spin/valley density wave. If the translation symmetry is intact, the identity representation $\mathbf{1}$ is the chemical potential, and the representation $\mathbf{15}$ represents the degenerate spin/valley magnetism.

Furthermore, a nonzero ϕ explicitly breaks the $SU(4)_f$ symmetry down to $SU(2)_s \times U(1)_v$ symmetry, as mentioned above. The degeneracy between the superconducting orders and particle-hole orders is all broken. We can use the valley quantum number $L_z = -1, 0, 1$ and total spin quantum

TABLE I. The correspondence between the orders in both particle-particle and particle-hole channels at $\phi = 0$ and $\phi = \pi/3$ under the flux insertion G. The loop current order we discuss in this work is the intravalley CDW order.

Flux	Intervalley pairing	Intravalley pairing	Intervalley density wave	Intravalley density wave
$\phi = 0$	$\mathbf{Q} = 0$ SC	$\mathbf{Q} = 0$ SC	$\mathbf{Q} = \mathbf{M}$ SDW/CDW	$\mathbf{Q} = \mathbf{M}$ SDW/CDW
$\phi = \pi/3$	$\mathbf{Q} = 0$ SC	$\mathbf{Q} = \pm\mathbf{K}$ PDW	$\mathbf{Q} = \mathbf{M} \pm \mathbf{K}$ SDW/CDW	$\mathbf{Q} = \mathbf{M}$ SDW/CDW

number of the Cooper pair to label the superconducting orders. In other words, we will have spin singlet or triplet pair with $L_z = -1, 0, 1$. The particle-hole orders are divided into spin orders and charge orders.

IV. CONVENTIONAL VAN HOVE SINGULARITIES: SIX PATCH MODEL

In this section, we focus on the $N_f = 2$ and $\phi = \pi/3$ case of Eq. (1). The Fermi surface at Van Hove doping is shown in Fig. 1. There are six conventional Van Hove singularities with log-divergent density of states. Interestingly, the physics for $\phi = 0$ and $\phi = \pi/3$ are closely connected with each other. Concretely, there is an invertible local transformation between the systems in Eq. (1) with $\phi = 0$ and $\pi/3$ at Van Hove doping, which is proposed in Ref. [74] for the single flavor case, i.e., $N_f = 1$ of Eq. (1). This local transformation guarantees that there is a one-to-one correspondence between the orders at $\phi = 0$ and $\phi = \pi/3$. Below we first discuss this transformation, and then use pRG analysis to identify the leading orders at $\phi = \pi/3$. We find consistency with earlier results on $\phi = 0$ case, by virtue of the local transformation.

A. Flux insertion

Before we dive into the detailed calculations, it's worth noticing that the physics at $\phi = \pi/3$ is closely connected with that at $\phi = 0$. Actually, there exists a local transformation between $\phi = 0$ and $\phi = \pi/3$ by inserting π flux in each triangular plaquette and preserving the gauge choice of the kinetic energy in Eq. (1) of the lattice model. We label the transformation as G. The transformation G not only maps the Hamiltonian, which includes both the tight binding and the interaction terms, from $\phi = 0$ to $\pi/3$, but also the ground state orders. This implies that if we know the leading order at $\phi = 0$, we can immediately arrive at the leading order with $\phi = \pi/3$, which is just the order at $\phi = 0$ acted by G.

Concretely, the transformation G composes two parts. Starting from $\phi = 0$, we first do the particle hole transformation: $c_{v,\sigma}(i) \rightarrow c_{v,\sigma}^\dagger(i)$, which inserts π flux in each plaquette and the filling is changed from n to $4 - n$, where n is the number of fermions per site. Then we perform the local gauge transformation

$$c_{v,\sigma}(j) \rightarrow e^{i\nu\eta_j} c_{v,\sigma}(j) \quad (3)$$

with $\eta_j = \mathbf{K} \cdot \mathbf{r}_j$ and $\mathbf{K} = (\frac{4\pi}{3}, 0)$, which preserves the gauge choice of the tight binding term in Eq. (1), such that the nearest-neighbor hopping terms along the \hat{a}_1 , \hat{a}_2 , and \hat{a}_3 directions have the same phase ϕ . In Fig. 2, we illustrate this gauge transformation on the lattice. This flux insertion G does not change the long-range hoppings and interactions we con-

sidered here, such as electron density interactions, Heisenberg exchange couplings, Hund couplings etc.

Since G is invertible, the orders at $\phi = 0$ and $\phi = \pi/3$ also have a one-to-one correspondence. The results is summarized in the Table I. We first apply G to the superconducting orders. If we start from one valley polarized component of the valley-triplet uniform pairing at $\phi = 0$: $\Delta(\mathbf{r}_i - \mathbf{r}_j)c_{+,\sigma}(i)(i\sigma_y)_{\sigma,\sigma'}c_{+,\sigma'}(j)$. This is uniform pairing as the pairing amplitude only depends on the relative coordinate $\mathbf{r}_i - \mathbf{r}_j$, which is invariant under the lattice translation symmetry. This pairing amplitude can have any form factors with respect to the relative coordinates, such as the s -wave, d -wave, etc. This order is mapped to the PDW order at $\phi = \pi/3$ under the transformation G:

$$\Delta(\mathbf{r}_i - \mathbf{r}_j)e^{-i\mathbf{K} \cdot \frac{\mathbf{r}_i + \mathbf{r}_j}{2}} c_{+,\sigma}^\dagger(i)(i\sigma_y)_{\sigma,\sigma'}c_{+,\sigma'}^\dagger(j), \quad (4)$$

of which the pairing amplitude gains a phase factor $e^{i\frac{2\pi}{3}}$ under the elementary lattice translation. Similarly, the valley polarized component polarized with the other valley is mapped to the finite momentum pairing with \mathbf{K} in Eq. (4) replaced with $-\mathbf{K}$. However, the intervalley pairing component $\Delta_{+-}(\mathbf{r}_i - \mathbf{r}_j)c_{+,\sigma}(i)(i\sigma_y)_{\sigma,\sigma'}c_{-,\sigma'}(j)$ is mapped to intervalley uniform pairing at $\phi = \pi/3$.

This flux insertion operation G enables us to know the orders at $\phi = \pi/3$ from the results at $\phi = 0$. Previous parquet RG calculations [33], functional RG (fRG) calculations [75] and mean field calculations [73] on the SU(4) Hubbard model on the triangular lattice with $\phi = 0$ have revealed that the superconducting order near the Van Hove doping has the chiral d -wave valley polarized component. The superconducting instability is the leading instability if the system is away from the perfect nesting limit, which is realized by introducing a finite next-nearest-neighbor hopping t' or a finite doping from the perfect nesting. Using the flux insertion G above, we can immediately arrive at the conclusion that chiral d -wave PDW order becomes the leading instability at $\phi = \pi/3$ away from the perfect nesting limit. The previous RG calculations with

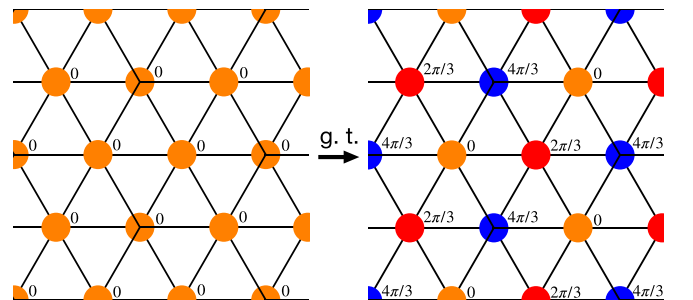


FIG. 2. Real space illustration of the local gauge transformation defined in Eq. (3).

$\phi = 0$ are reliable in the weak and moderate coupling regime, which means the chiral d -wave PDW also exists at least in this regime for $\phi = \pi/3$.

We briefly discuss whether the PDW order is present at other fillings with $\phi = \pi/3$. The flux insertion operation G is applicable to any fillings. As a result, if the valley polarized uniform pairing is favored at $\phi = 0$ and filling n , then the PDW order will also be the leading order at $\phi = \pi/3$ and filling $4-n$, regardless of whether the Van Hove singularities are present or not. If the fermion interaction at $\phi = 0$ preserves the $SU(4)$ symmetry, such as the Hubbard or Heisenberg interaction, then the Kohn-Luttinger instability will always become the leading instability with repulsive interactions at generic fillings. Further, recalling the representation decomposition of $SU(4)$: $\mathbf{4} \otimes \mathbf{4} = \mathbf{6} \oplus \mathbf{10}$, the valley polarized pairing is always degenerate with other pairings in both the representation $\mathbf{6}$ and $\mathbf{10}$. This means that the PDW order is always present at $\phi = \pi/3$ with repulsive $SU(4)$ preserving interactions, due to the Kohn-Luttinger instability at $\phi = 0$. Moreover, from the fRG calculations in Ref. [75], the valley triplet pairing can be favored as the unique leading instability in a certain regime of additional $SU(4)$ breaking Hund couplings, so the PDW order at $\phi = \pi/3$ will also exist in the same coupling parameter regime with additional $SU(4)$ breaking Hund couplings. To sum up, the PDW order at $\phi = \pi/3$ is not fine tuned to the Van Hove doping, but is a stable phase at generic fillings with repulsive interactions.

There is another interesting state, i.e., loop current phase, near Van Hove doping reported in previous RG calculations at $\phi = 0$ [33,75]. If the Fermi surface is nearly perfectly nested, the loop current phase will be favored as the leading instability by the repulsive Hubbard interaction and Heisenberg interaction. The order parameter of the loop current phase is the imaginary CDW order, which spontaneously breaks the time reversal symmetry, and induces a $\pi/2$ or $-\pi/2$ flux in each triangle plaquette. We can also use the flux insertion argument to construct the corresponding order at $\phi = \pi/3$ with repulsive Hubbard and Heisenberg interaction at Van Hove doping and a nearly perfect nested Fermi surface. The order parameter of the loop current order at $\phi = 0$ is [33,75]

$$\Delta_{\text{loop current}} = \sum_{k,a} f_a(\mathbf{k}) \hat{c}^\dagger(\mathbf{k} + \mathbf{M}_a) c(\mathbf{k}), \quad (5)$$

where the sum over spin and valley is implicitly assumed henceforth. \mathbf{M}_a with $a = 1, 2, 3$ are the three momenta of the Van Hove singularities of the tight binding model \hat{H}_0 of Eq. (1). The three form factors f_a preserve the C_3 rotation symmetry and ensure that the expectation value of the order parameter in Eq. (5) is purely imaginary. For example, it is fitted as: $f_1 = 2 \sin(k_x/2) \sin(\sqrt{3}k_y/2)$, $f_{2,3} = \mp \cos(k_x) \pm \cos((k_x \pm \sqrt{3}k_y)/2)$ from the vertex obtained in fRG calculations [75]. Now we apply the flux insertion operator G , and the order parameter $\Delta_{\text{loop current}}$ becomes

$$\begin{aligned} \Delta_{\phi=\pi/3} &= - \sum_{k,a,v} f_a(\mathbf{k}) \hat{c}_v^\dagger(\mathbf{k} + \mathbf{M}_a + v\mathbf{K}) c_v(\mathbf{k} + v\mathbf{K}) \\ &= - \sum_{k,a,v} f_a(\mathbf{k} + v\mathbf{K}) \hat{c}_v^\dagger(\mathbf{k} + \mathbf{M}_a) c_v(\mathbf{k}), \end{aligned} \quad (6)$$

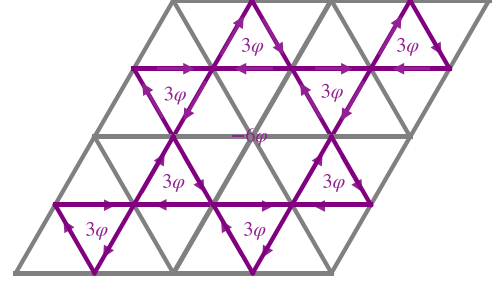


FIG. 3. Kagome flux pattern of the loop current order at $\phi = \pi/3$. The flux of each triangle plaquette is 3ϕ , and the flux of each hexagon plaquette is -6ϕ . For the pure imaginary CDW order $\phi = \pi/2$.

where $v = \pm$ is the index of the valley. The order parameter $\Delta_{\phi=\pi/3}$ is still the pure imaginary CDW order. The real space flux pattern at $\phi = \pi/3$ is shown in Fig. 3.

As a result, the leading instability at $\phi = \pi/3$ is still the loop current phase with repulsive Hubbard and Heisenberg interaction near Van Hove doping. However, this is true with a nearly perfect nested Fermi surface. If we dope this loop current phase or induce a t' beyond a critical value to destroy the nesting, the loop current phase will become the degenerate chiral d -wave PDW order and uniform SC order. This phase transition corresponds to the transition from the loop current phase to chiral d -wave uniform SC order at $\phi = 0$ [33,75].

B. Bare susceptibilities

The flux insertion argument above is specific to the lattice model like (1). In cases when there lacks the information of the low-energy lattice model, one can still apply the RG analysis to study the competing orders.

The first step is to identify the building blocks for parquet RG, which are various particle-hole and particle-particle susceptibilities:

$$\begin{aligned} \Pi_{\text{ph}}(\mathbf{P}, T) &= -T \sum_n \int \frac{d^2k}{(2\pi)^2} G_0(\omega_n, k) G_0(\omega_n, \mathbf{P} + k), \\ \Pi_{\text{pp}}(\mathbf{P}, T) &= T \sum_n \int \frac{d^2k}{(2\pi)^2} G_0(\omega_n, k) G_0(-\omega_n, \mathbf{P} - k), \end{aligned} \quad (7)$$

where $G_0(\omega_n, q) = \frac{1}{i\omega_n - \epsilon(q)}$ and $\omega_n = (2n + 1)\pi T$ is the fermion frequency. The leading divergent susceptibility is used as the flowing energy scale, with infrared limit $T \rightarrow 0$, in the parquet RG formalism.

We take the six patch model near the six Van Hove singularities with the patch size Λ . There are three kinds of \ln^2 divergent susceptibilities: $\Pi_{\text{pp}}(0, T)$, $\Pi_{\text{pp}}(\pm\mathbf{K}, T)$, and $\Pi_{\text{ph}}(\mathbf{Q}_\pm, T)$.

$$\begin{aligned} \Pi_{\text{pp}}(0, T) &= \frac{1}{4\sqrt{3}\pi^2 t} \ln \frac{\Lambda}{\max\{T, \mu\}} \ln \frac{\Lambda}{T}, \\ \Pi_{\text{pp}}(\pm\mathbf{K}, T) &= \frac{1}{4\sqrt{3}\pi^2 t} \ln \frac{\Lambda}{\max\{T, \mu\}} \ln \frac{\Lambda}{T}, \end{aligned}$$

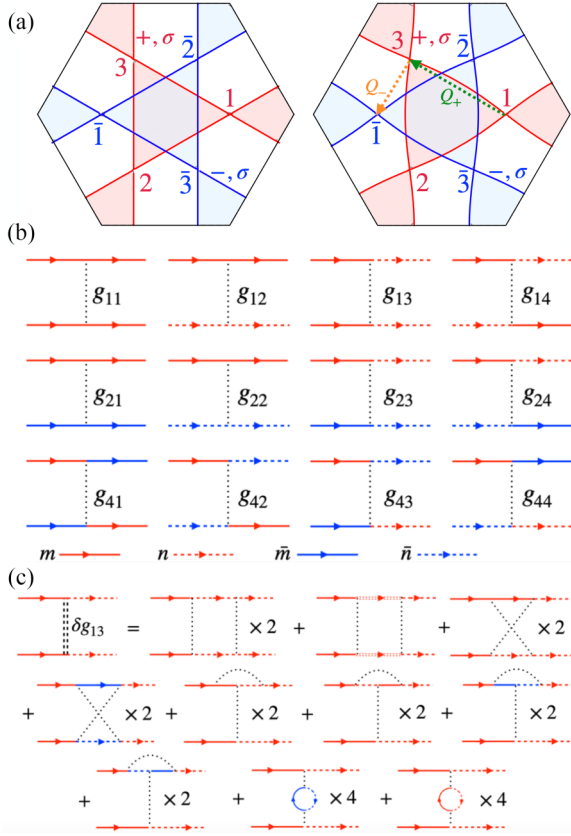


FIG. 4. (a) The left panel is the Fermi surface at Van Hove doping with $t' = 0$; the right panel is the Fermi surface at Van Hove doping with $t' = 0.1$. The location of the Van Hove singularities are not changed with nonzero t' . The momentum vectors \mathbf{Q}_+ and \mathbf{Q}_- are the particle-hole nesting vectors, at which the bare p-h susceptibilities diverge in \ln^2 manner. The red and blue colors represent the two valleys with opposite flux. (b) All the twelve symmetry allowed independent four fermion interactions. The red and blue colors represent the opposite valleys and the solid and dashed lines represent different patches within the same valley. (c) Diagrammatic representation of the renormalization of the interaction g_{13} by the particle-particle and particle-hole bubbles defined in Eq. (8).

$$\Pi_{ph}(\mathbf{Q}_{\pm}, T) = \frac{1}{8\sqrt{3}\pi^2 t} \ln \frac{\Lambda}{\max\{T, \mu\}} \ln \frac{\Lambda}{\max\{T, \mu, t'\}}. \quad (8)$$

Here the momentum \mathbf{Q}_{\pm} are depicted in Fig. 4(a). We see that \mathbf{Q}_+ connects patches within the same valley, while \mathbf{Q}_- connects patches from opposite valleys. The detailed calculations of Eq. (8) are presented in Appendix A. This is also expected from the flux insertion argument. The only two \ln^2 divergent bare susceptibilities for $\phi = 0$ are $\Pi_{pp}(0, T)$, $\Pi_{ph}(\mathbf{M}, T)$; after the flux insertion transformation \mathbf{G} : $\phi = 0 \rightarrow \phi = \pi/3$, the susceptibilities of the same valley and opposite valleys are mapped into those corresponding to different orders. Concretely, the particle-particle susceptibilities of the same and opposite valleys are mapped into $\Pi_{pp}(0, T)$ and $\Pi_{pp}(\pm\mathbf{K}, T)$ respectively; the particle-hole susceptibilities of the same and opposite valleys are mapped into $\Pi_{ph}(\mathbf{Q}_+, T)$ and $\Pi_{ph}(\mathbf{Q}_-, T)$ respectively.

Note that even with a finite t' and/or finite doping (chemical potential), we still have $\Pi_{pp}(\pm\mathbf{K}, T) = \Pi_{pp}(0, T)$ and $\Pi_{ph}(\mathbf{Q}_+, T) = \Pi_{ph}(\mathbf{Q}_-, T)$. The comparison between cases with and without t' is also shown in Fig. 4(a), which shows that the particle-particle FS nesting is immune to the presence of a finite t' , consistent with Eq. (8). This enables us to use a single parameter $d = \frac{\Pi_{ph}(\mathbf{Q}_{\pm}, T)}{\Pi_{pp}(0, T)}$ to characterize the degree of nesting in our following RG analysis. Note that for hexagonal lattices as we considered in the current work, the maximum value of d is $1/2$, which is different from the square lattice case, where the maximum of d is 1.

C. RG for interactions

There are twelve inequivalent symmetry-allowed four fermion interactions in the six patch case with $N_f = 2$, which we show in Fig. 4(b). We label all the interactions as g_{ij} , where $i = 1, 2, 4$ and $j = 1, 2, 3, 4$. Note $j = 1, 2$ represent forward scattering of the valley and patch degrees of freedom, while $j = 3$ and 4 represent umklapp and backward scattering respectively. The valley umklapp interactions are forbidden by momentum conservation. However, other than this, all the left twelve interactions are allowed. The three interactions g_{13} , g_{24} , g_{44} are umklapp scatterings, which show up only in the special case when $\phi = \pi/3$, and are absent for a general ϕ in the previous studies of similar systems [33,34]. As a result, the stable PDW phases are absent in these studies. The valley preserving interactions g_{1i} and g_{2i} can arise from the SU(4) symmetric lattice interactions such as Hubbard and Heisenberg interactions. The valley flipping interactions g_{4i} can result from the SU(4) broken Hund couplings on the lattice. Meanwhile, the Heisenberg interaction also gives anisotropic initial values of g_{1i} and g_{2i} . Here, given that these different interactions are generally present in the system, we discuss the phase diagram from general initial values of the g_{ij} , instead of the original form of the interactions defined in Eq. (2). The projections of different lattice interactions U , J , V_h , and K in Eq. (2) to g_{ij} are recorded in Appendix B.

The one loop parquet RG equations for all the twelve interactions can be obtained using the diagrammatic technique. As an example, we show the renormalization of g_{13} in Fig. 4(c); the renormalization for other interactions can be obtained similarly. Defining $\dot{g}_{ij} = dg_{ij}/dy$, where $y = \Pi_{pp}(0, T)$ and using $d = \frac{d\Pi_{ph}(\mathbf{Q}_{\pm}, T)}{y} \approx d(y_c)$, where y_c is the critical value at which at least one of g_{ij} diverges, we arrive at

$$\begin{aligned} \dot{g}_{11} &= -g_{11}^2 - 2g_{13}^2, & \dot{g}_{12} &= d(g_{12}^2 + g_{13}^2 + g_{43}^2 + g_{44}^2), \\ \dot{g}_{13} &= -2g_{13}g_{11} - g_{13}^2 + 4d(g_{12}g_{13} - g_{23}g_{24}) \\ &\quad + 2d(g_{23}g_{44} + g_{24}g_{43} + g_{43}g_{44} - g_{13}g_{14}), \\ \dot{g}_{14} &= 2d(g_{12}g_{14} + g_{24}g_{44} + g_{23}g_{43} - g_{24}^2 - g_{14}^2 - g_{23}^2), \\ \dot{g}_{21} &= -g_{21}^2 - 2g_{23}^2 - g_{41}^2 - 2g_{43}^2, & \dot{g}_{22} &= d(g_{22}^2 + g_{23}^2), \\ \dot{g}_{23} &= -2g_{23}g_{21} - g_{23}^2 \\ &\quad + 2d(g_{23}g_{22} + g_{12}g_{23} - 2g_{23}g_{14} - g_{13}g_{24}) \\ &\quad - (2g_{41}g_{43} + g_{43}^2) + 2d(g_{13}g_{44} + g_{14}g_{43}), \end{aligned}$$

$$\begin{aligned}
 \dot{g}_{24} &= 2d(g_{12}g_{24} + g_{14}g_{44} + g_{13}g_{43} - g_{13}g_{23} - 2g_{24}g_{14}), \\
 \dot{g}_{41} &= -2(g_{21}g_{41} + 2g_{23}g_{43}), \\
 \dot{g}_{42} &= 2d(g_{22}g_{42} + g_{23}g_{43} - g_{43}^2 - g_{42}^2), \\
 \dot{g}_{43} &= -2(g_{21}g_{43} + g_{23}g_{41} + g_{23}g_{43}) \\
 &\quad + 2d(g_{12}g_{43} + g_{13}g_{44} + g_{22}g_{43} + g_{23}g_{42} - 2g_{42}g_{43}), \\
 \dot{g}_{44} &= 2d(g_{12}g_{44} + g_{13}g_{43}). \tag{9}
 \end{aligned}$$

We are interested in the stable strong coupling fixed points starting from different interactions, which correspond to the symmetry breaking ground states. Physically, the stable fixed points, or fixed trajectories mean that the corresponding ordered phases need no fine tuning of the interactions and exist in a wide parameter space. The asymptotic behavior of the fixed trajectories in the one-loop RG equations is

$$g_{ij} \approx \frac{G_{ij}}{y_c - y}. \tag{10}$$

Therefore, if G_{ij} is nonzero, g_{ij} diverges when y approaches y_c from below, i.e., it either flows to strong repulsion or strong attraction. We also notice that, for different g_{ij} , the critical value y_c might not be the same. In cases we have different y_c , apparently the smallest one corresponds to the onset of instabilities. In that case, for those g_{ij} which diverge at a larger y_c , their effective contributions vanish at the smallest y_c where they are still small and can be neglected. To examine the spontaneous symmetry breaking orders corresponding to the stable fixed trajectories, one needs to look into the order parameter vertices and susceptibilities under RG flow, which we discuss below.

D. RG for order parameters

Having established the RG flow for the four fermion interactions g_{ij} , the competition among different orders can be readily identified. To this end, we need to write down the order parameters, and inspect how they flow when g_{ij} changes with the energy scale. They can be well seen from calculating the triple vertex functions associated with each order parameter. The order parameter whose vertex and susceptibility diverge most quickly is the leading instability under the given interactions which are set as the initial values of the four fermion interactions g_{ij} . Below we analyze each order separately.

1. Pair density wave

We start from the pair density wave pairing orders. The renormalization of the corresponding vertices are shown in Fig. 5. Note that the vertices of the PDW order have three components. The three components correspond to three classes of paired patches, which are related with each other by C_3 rotation. Corresponding to different superconducting form factors (such as s -wave, d -wave, etc.), the vertices can take different values on these different patches, and the leading instability is a combination from different patches [31].

In Fig. 5, the spin configuration is $i\sigma_y$ which corresponds to spin singlet pairing. This is because the PDW order can only be spin-singlet with total valley quantum number $|L_z| = 1$ in our six patch model. This is due to that the vertex of spin-

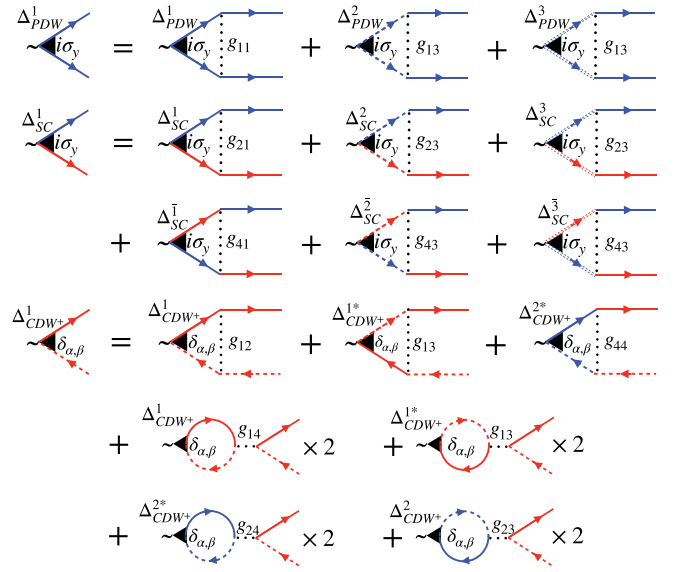


FIG. 5. Diagrammatic representations of the one loop corrections to all the possible superconducting vertices and charge density wave order with nesting momentum \mathbf{Q}_+ of the six patch model. The superconducting orders include the PDW and uniform SC. The red and blue colors represent the two valleys with opposite flux. The vertex of the uniform SC can be either spin singlet or triplet, and their diagrams are the same. As a result, the spin singlet and triplet pairings with $L_z = 0$ are always degenerate. The imaginary part of the CDW vertex is the loop current vertex.

triplet pair with momentum \mathbf{K} is actually zero:

$$\begin{aligned}
 \Delta_{\text{PDW-triplet}} &= \sum_{k,a=1,2,3} c_a^\dagger(\mathbf{k}) i\sigma_y \vec{\sigma} [c_a^\dagger(-\mathbf{k})]^T + \text{H.c.} \\
 &= -\Delta_{\text{PDW-triplet}} \sum_{k,a=1,2,3} c_a^\dagger(-\mathbf{k}) i\sigma_y \sigma [c_a^\dagger(\mathbf{k})]^T + \text{H.c.} \\
 &= -\Delta_{\text{PDW-triplet}} \sum_{k,a=1,2,3} c_a^\dagger(\mathbf{k}) i\sigma_y \sigma [c_a^\dagger(-\mathbf{k})]^T + \text{H.c.}, \tag{11}
 \end{aligned}$$

where a is the patch label, and \mathbf{k} is the momentum lies in a patch near each Van Hove singularity. Meanwhile, the patch is inversion symmetric with respect to the inversion center at the Van Hove singularity. The two-component spinor operator $c_a^\dagger(\mathbf{k})$ is: $c_a^\dagger(\mathbf{k}) = (c_{a,\uparrow}^\dagger(\mathbf{k}), c_{a,\downarrow}^\dagger(\mathbf{k}))$. Similarly, we can also prove that the spin triplet PDW vertex with nesting momentum $-\mathbf{K}$ is also zero. As a result, the spin triplet PDW order is expected to be energetically unfavored even if the whole Fermi surface is taken into consideration, as this order parameter cannot gap out the Van Hove singularity.

We next identify the pairing symmetry of the leading instability. Explicitly, the PDW vertex RG equations corresponding to the diagrammatics in Fig. 5 are

$$\begin{pmatrix} \dot{\Delta}_{\text{PDW}}^1 \\ \dot{\Delta}_{\text{PDW}}^2 \\ \dot{\Delta}_{\text{PDW}}^3 \end{pmatrix} = - \begin{pmatrix} g_{11} & g_{13} & g_{13} \\ g_{13} & g_{11} & g_{13} \\ g_{13} & g_{13} & g_{11} \end{pmatrix} \begin{pmatrix} \Delta_{\text{PDW}}^1 \\ \Delta_{\text{PDW}}^2 \\ \Delta_{\text{PDW}}^3 \end{pmatrix}. \tag{12}$$

If we diagonalize the three by three coefficient matrix in Eq. (12), we will arrive at three eigenfunctions corresponding

to s -wave and two degenerate d -wave superconducting orders. Their eigen RG equations are

$$\begin{aligned}\Delta_{\text{PDW}}^s &= (1, 1, 1) : \dot{\Delta}_{\text{PDW}}^s = -(g_{11} + 2g_{13})\Delta_{\text{PDW}}^s, \\ \Delta_{\text{PDW}}^{d_1} &= \frac{\sqrt{2}}{3}(1, -1/2, -1/2) : \dot{\Delta}_{\text{PDW}}^{d_1} = -(g_{11} - g_{13})\Delta_{\text{PDW}}^{d_1}, \\ \Delta_{\text{PDW}}^{d_2} &= \frac{1}{\sqrt{2}}(0, 1, -1) : \dot{\Delta}_{\text{PDW}}^{d_2} = -(g_{11} - g_{13})\Delta_{\text{PDW}}^{d_2}.\end{aligned}\quad (13)$$

Note that the two d -wave orders are degenerate, which is manifest in the coefficients $-(g_{11} - g_{13})$ in the RG equations of $\Delta_{\text{PDW}}^{d_{1,2}}$ in Eq. (13). The degeneracy is guaranteed by the underlying lattice symmetry C_{3v} , as the two d -wave orders belong to the same two-dimensional representation E. The ground state favors the chiral combination of these two components: $\Delta_{\text{PDW}}^{d_1} \pm i\Delta_{\text{PDW}}^{d_2}$, which can be verified through the Ginzburg-Landau free energy analysis similar to the three patch model in hexagonal systems [31].

2. Uniform superconductivity

The vertices equations of uniform superconducting orders are more involved because there are six components of the uniform superconducting vertex. The spin singlet and triplet uniform pairings are degenerate, and the SS (TT) pairing can mix with TS (ST) pairing in principle due to the broken $SU(2)_v$ valley symmetry. The vertex RG equations for the uniform SC order is

$$\begin{pmatrix} \dot{\Delta}_{\text{SC}}^1 \\ \dot{\Delta}_{\text{SC}}^2 \\ \dot{\Delta}_{\text{SC}}^3 \\ \dot{\Delta}_{\text{SC}}^{\bar{1}} \\ \dot{\Delta}_{\text{SC}}^{\bar{2}} \\ \dot{\Delta}_{\text{SC}}^{\bar{3}} \end{pmatrix} = - \begin{pmatrix} g_{21} & g_{23} & g_{23} & g_{41} & g_{43} & g_{43} \\ g_{23} & g_{21} & g_{23} & g_{43} & g_{41} & g_{43} \\ g_{23} & g_{23} & g_{21} & g_{43} & g_{43} & g_{41} \\ g_{41} & g_{43} & g_{43} & g_{21} & g_{23} & g_{23} \\ g_{43} & g_{41} & g_{43} & g_{23} & g_{21} & g_{23} \\ g_{43} & g_{43} & g_{41} & g_{23} & g_{23} & g_{21} \end{pmatrix} \begin{pmatrix} \Delta_{\text{SC}}^1 \\ \Delta_{\text{SC}}^2 \\ \Delta_{\text{SC}}^3 \\ \Delta_{\text{SC}}^{\bar{1}} \\ \Delta_{\text{SC}}^{\bar{2}} \\ \Delta_{\text{SC}}^{\bar{3}} \end{pmatrix}.\quad (14)$$

We arrive at different eigen pairing functions with different form factors and flavor quantum number by diagonalizing the six by six coefficient matrix in Eq. (14):

$$\begin{aligned}\Delta_{\text{sc}}^s &= (1, 1, 1, 1, 1, 1) : \\ \dot{\Delta}_{\text{sc}}^s &= -(g_{21} + 2g_{23} + g_{41} + 2g_{43})\Delta_{\text{sc}}^s,\end{aligned}$$

$$\begin{aligned}\Delta_{\text{sc}}^f &= (1, 1, 1, -1, -1, -1) : \\ \dot{\Delta}_{\text{sc}}^f &= -(g_{21} + 2g_{23} - g_{41} - 2g_{43})\Delta_{\text{sc}}^f,\end{aligned}$$

$$\begin{aligned}\Delta_{\text{sc}}^{d_1, d_2} &= 1/2(0, 1, -1, 0, 1, -1), \\ &\frac{1}{\sqrt{3}}(1, -1/2, -1/2, 1, -1/2, -1/2) : \\ \dot{\Delta}_{\text{sc}}^{d_1, d_2} &= -(g_{21} - g_{23} + g_{41} - g_{43})\Delta_{\text{sc}}^{d_1, d_2},\end{aligned}$$

$$\begin{aligned}\Delta_{\text{sc}}^{p_1, p_2} &= (1, 0, -1, -1, 0, 1), (1, -1, 0, -1, 1, 0) : \\ \dot{\Delta}_{\text{sc}}^{p_1, p_2} &= -(g_{21} - g_{23} - g_{41} + g_{43})\Delta_{\text{sc}}^{p_1, p_2},\end{aligned}\quad (15)$$

where Δ_{sc}^f is the vertex of f -wave uniform pairing. And $\Delta_{\text{sc}}^{p_1, p_2}$ are the vertices of p -wave uniform pairing, which belong to the two-dimensional E representation of C_{3v} . These two superconducting orders are TT or SS pairings with odd parity form factors. The remaining two vertices are TS or ST pairings with even parity form factors. Δ_{sc}^s is the vertex of s -wave uniform pairing. $\Delta_{\text{sc}}^{d_1, d_2}$ are the vertices of d -wave uniform pairing, which also belong to the E representation.

3. Charge density wave

Now we move to the charge density wave vertices with nesting momentum \mathbf{Q}_{\pm} . We will use CDW^{\pm} to denote charge-density waves with momentum \mathbf{Q}_{\pm} . The CDW^+ vertex contains both real and imaginary parts, each of which has two components, corresponding to two valleys with opposite fluxes. The one loop RG equations of the density wave orders can be obtained using similar diagrammatics shown in Fig. 5. The resulting equations are

$$\begin{pmatrix} \dot{\Delta}_{\text{ReCDW}^+}^1 \\ \dot{\Delta}_{\text{ReCDW}^+}^2 \end{pmatrix} = d \begin{pmatrix} a & b \\ b & a \end{pmatrix} \begin{pmatrix} \Delta_{\text{ReCDW}^+}^1 \\ \Delta_{\text{ReCDW}^+}^2 \end{pmatrix},$$

$$\begin{pmatrix} \dot{\Delta}_{\text{ImCDW}^+}^1 \\ \dot{\Delta}_{\text{ImCDW}^+}^2 \end{pmatrix} = d \begin{pmatrix} e & f \\ f & e \end{pmatrix} \begin{pmatrix} \Delta_{\text{ImCDW}^+}^1 \\ \Delta_{\text{ImCDW}^+}^2 \end{pmatrix},\quad (16)$$

$$\begin{pmatrix} \dot{\Delta}_{\text{CDW}^-}^1 \\ \dot{\Delta}_{\text{CDW}^-}^2 \end{pmatrix} = d \begin{pmatrix} g_{22} - 2g_{42} & g_{23} - 2g_{43} \\ g_{23} - 2g_{43} & g_{22} - 2g_{42} \end{pmatrix} \begin{pmatrix} \Delta_{\text{CDW}^-}^1 \\ \Delta_{\text{CDW}^-}^2 \end{pmatrix}.\quad (17)$$

In Eq. (16), we have introduced the following quantities for brevity:

$$\begin{aligned}a &= g_{12} - 2g_{14} - g_{13}, & b &= -2g_{24} - 2g_{23} + g_{43} + g_{44}, \\ e &= g_{12} - 2g_{14} + g_{13}, & f &= 2g_{24} - 2g_{23} + g_{43} - g_{44}.\end{aligned}\quad (18)$$

Like in the superconducting case, here we also need to diagonalize all the two-by-two matrices in the vertex equations of charge density wave order to find the leading instability configuration. Interestingly, despite of different order parameters, all these matrices contain only two distinct elements: the diagonal entry h_{11} and the off-diagonal entry h_{12} , since the two diagonal (off-diagonal) entries have identical values. Matrix of this type has eigenvalues $h_{11} \pm h_{12}$, with the corresponding eigenfunctions being $\Delta_{\text{CDW}}^{e,o} = \Delta_{\text{CDW}}^1 \pm \Delta_{\text{CDW}}^2$ with $e(o)$ standing for even (odd).

4. Spin density wave order

The spin density wave momentum \mathbf{Q}_{\pm} is also one of the competing orders. Similar to the charge density wave order, the spin density wave with momentum \mathbf{Q}_{\pm} has real and imaginary parts. The vertex RG equations of spin density wave orders are

$$\begin{pmatrix} \dot{\Delta}_{\text{ReSDW}^+}^1 \\ \dot{\Delta}_{\text{ReSDW}^+}^2 \end{pmatrix} = d \begin{pmatrix} g_{12} + g_{13} & g_{43} + g_{44} \\ g_{43} + g_{44} & g_{12} + g_{13} \end{pmatrix} \begin{pmatrix} \Delta_{\text{ReSDW}^+}^1 \\ \Delta_{\text{ReSDW}^+}^2 \end{pmatrix},$$

$$\begin{pmatrix} \dot{\Delta}_{\text{ImSDW}^+}^1 \\ \dot{\Delta}_{\text{ImSDW}^+}^2 \end{pmatrix} = d \begin{pmatrix} g_{12} - g_{13} & g_{43} - g_{44} \\ g_{43} - g_{44} & g_{12} - g_{13} \end{pmatrix} \begin{pmatrix} \Delta_{\text{ImSDW}^+}^1 \\ \Delta_{\text{ImSDW}^+}^2 \end{pmatrix},\quad (19)$$

$$\begin{pmatrix} \Delta_{\text{SDW}^-}^1 \\ \Delta_{\text{SDW}^-}^2 \end{pmatrix} = d \begin{pmatrix} g_{22} & g_{23} \\ g_{23} & g_{22} \end{pmatrix} \begin{pmatrix} \Delta_{\text{SDW}^-}^1 \\ \Delta_{\text{SDW}^-}^2 \end{pmatrix}. \quad (20)$$

The two by two coefficient matrix of each spin density wave vertex has similar structure to that of the charge density wave order. As a result, the eigenfunctions are $\Delta_{\text{SDW}}^{e,o} = \Delta_{\text{SDW}}^1 \pm \Delta_{\text{SDW}}^2$ with corresponding eigenvalues $h_{11} \pm h_{12}$.

E. The phase diagram from RG analysis

Finally, we are in the position to determine the leading order by calculating the renormalized susceptibilities of both the superconducting and the density wave order, which are governed by the following equations [33,76]:

$$\dot{\chi}_{\text{SC}} = |\Delta_{\text{SC}}|^2, \quad \dot{\chi}_{\text{DW}} = d|\Delta_{\text{DW}}|^2. \quad (21)$$

Note here Δ_{SC} includes both PDW and uniform SC orders. From the equations of vertices in the particle-particle and particle-hole channel, we can obtain the asymptotic solutions $\Delta_{\text{SC/DW}}(y) \approx (y_c - y)^{\beta_{\text{SC/DW}}}$, which is valid near y_c . Substituting this form into Eq. (21) we obtain the asymptotic solution for χ , which behaves like $\chi(y) \approx (y_c - y)^\alpha$ [33,76–78] and the exponent can be obtained via

$$\alpha_{\text{SC/DW}} = 2\beta_{\text{SC/DW}} + 1. \quad (22)$$

If for some channel $\alpha < 0$, the corresponding susceptibility diverges and signals an instability. The susceptibility with the most negative α is therefore the leading instability when reducing energy scale. It is obvious that α in the density wave channel depends on the nesting parameter d . If d is small, β_{DW} is suppressed and hence α_{DW} becomes positive and there is no onset of density wave order. This is expected since a smaller d indicates that the FS nesting in the particle-hole channel is less important. The superconducting orders, however, are almost immune to this destruction.

In Fig. 6, we present the phase diagram obtained for various initial interactions as well as nesting parameters. For each group of parameters, we show the phase boundary on the left panel, and the color map of y_c on the right panel. We first focus on the perfect nesting limit $d = 1/2$, where not only the superconducting order, but also density wave orders are found. When the inter-patch interactions g_{4j} are neglected, we find, in addition to PDW and SC orders, an imaginary CDW order with momentum \mathbf{Q}_+ near the SU(4) symmetric line: $g_{1i} = g_{2i} > 0$ [see Figs. 6(a) and 6(b)]. Since there are in fact 3 different \mathbf{Q}_+ related by C_3 rotation, this imaginary CDW is in the $3\mathbf{Q}_+$ state which gives rise to loop current order [79], and, similar to Haldane's model, can host quantum anomalous Hall effect. A real space configuration of this loop current is shown in Fig. 3. The bond currents form a Kagome lattice pattern. This result is consistent with similar RG results at $\phi = 0$ [33,75]. The loop current order can be enhanced by the anisotropic g_{1i} , g_{2i} and attractive valley flipping g_{4i} [Figs. 6(b) and 6(d)]. The anisotropy of g_{1i} and g_{2i} can arise from the nearest-neighbour interactions on the lattice. The loop current order here is unstable against a valley-splitting magnetic field. This can be seen from the Fig. 5, the internal fermion loops contributed by the valley-umklapp interactions are prohibited by a nonzero valley-splitting magnetic field.

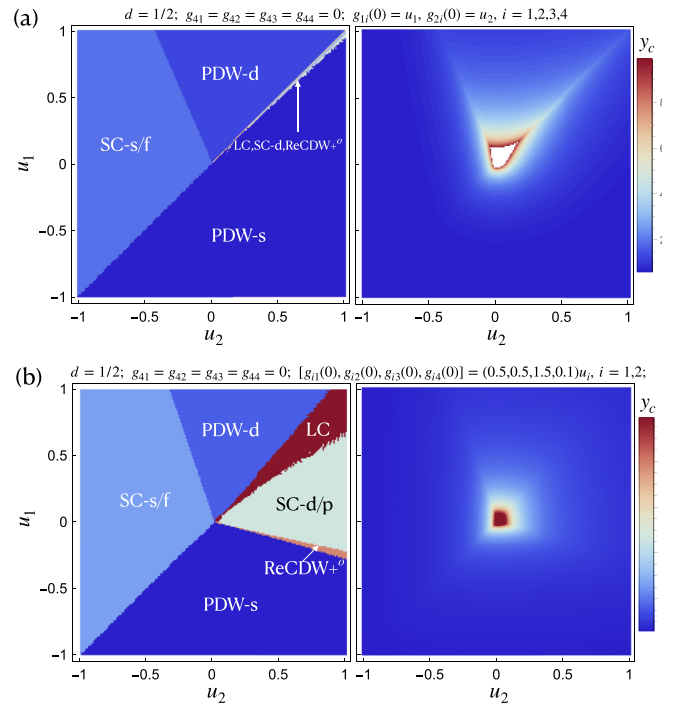


FIG. 6. The phase diagram and divergent energy scale of the six patch model at $\phi = \pi/3$. Each sub-figure consists of the phase diagram (left) and the corresponding y_c (right) obtained from the nesting parameter d and initial values g_{ij} labeled on the top. The transition temperature and the magnitude Δ of the order parameter can be estimated from y_c as [31,32] $T_c, \Delta \sim \Lambda e^{-1/\sqrt{y_c}}$, where $\nu = 4\sqrt{3}t\pi^2$ and Λ is the UV cutoff and is typically taken as t [31,32]. The color map only shows y_c up to $y_c = 10$, for $y_c > 10$, the areas are denoted by white color. (a) The phase diagram from the initial values: $g_{1j} = u_1$, $g_{2j} = u_2$, $g_{4j} = 0$, $j = 1, 2, 3, 4$ in the perfect nesting limit $d = 1/2$. The chiral d -wave PDW, s -wave PDW and degenerate s - and f -wave uniform pairing dominates nearly all regimes in the phase diagram. The loop current (LC) order occurs only near the SU(4) symmetric line with repulsive interactions: $g_{1i} = g_{2i} > 0$, which is accompanied by chiral d -wave SC as well as parity-odd real CDW with momentum \mathbf{Q}_+ . (b) The phase diagram from the anisotropic initial values of g_{1j} and g_{2j} and zero g_{4i} in the perfect nesting limit $d = 1/2$. The loop current order is enhanced by the anisotropic initial values and occupies a finite area in this regime.

Apart from the loop current order, the phase diagram for the six patch case is almost dominated by PDW and uniform SC orders. Among those, the most interesting order is the d -wave PDW. In hexagonal lattices, the d -wave order parameters belong to the two-dimensional irreducible representation of the lattice group. Therefore there are two degenerate d -wave states, and the true ground state must be obtained by comparing their Landau free energy. In most cases, the d -wave orders spontaneously break the time reversal symmetry to lower energy, leading to a chiral SC state. In our case, both the d -wave PDW and d -wave SC are chiral, with the order parameter being $\Delta_1 + i\Delta_2$ or $\Delta_1 - i\Delta_2$. It is worth to notice that, although the PDW we discussed here has both momentum \mathbf{K} and $-\mathbf{K}$, the Larkin-Ovchinnikov(LO) state, in which the magnitude of the gap function oscillates in space and therefore has nodal lines, is not energetically favored.

This is because the FS of each valley at $\phi = \pi/3$ has only one nesting vector in the particle-particle channel. Thus, our PDW discussed here is similar to the original Fulde-Ferrell state.

We have also confirmed that both the PDW and the uniform SC found here are indeed stable fixed points. To see this, one can include small perturbations around the fixed point and test whether the system flows away from this point. Formally this can be seen by examining the eigenvalues of the stability matrix discussed in Appendix E. Using this approach, we find that both the PDW and the uniform SC are stable against all kinds of symmetry allowed interactions. The fixed point corresponding to the loop-current order has two directions of relevant perturbations, which drive the RG flow to fixed points favoring nearby superconducting phases. However, the loop current susceptibility is still the leading one until the interactions flow beyond the perturbative regime: $\max|g_{ij}(y)| \gg 1$, in which case we have to stop the RG flow far before that energy scale. This means that the loop current order is still the stable phase in the regime of our phase diagram except in the weak coupling limit, where we can push the RG flow to the energy scale y_c at which the interactions really diverge [80].

To summarize, the orders that we find here, such as the loop current, the PDW and the uniform SC, are all consistent with the analysis performed in a $\phi = 0$ SU(4) model, in the sense that they can be connected by the local transformation discussed in Sec. IV A when a lattice model like Eq. (1) is available. However, our pRG results are quite general, and are applicable to the cases when there lacks the information of a lattice Hamiltonian. The key ingredients here are the presence of six CVHS, and the inclusion of the umklapp interactions g_{13} , g_{24} , and g_{44} .

F. Electronic properties of the d -wave PDW

In this section, we investigate the electronic properties of the d -wave PDW found by our parquet RG analysis through a mean field analysis. There are two kinds of d -wave intravalley PDW with chiral combinations of the two d -wave components d_1 and d_2 in Eq. (13) at $\phi = \pi/3$ in our phase diagram. The first kind of chiral d -wave PDW is connected to the uniform chiral d -wave uniform superconductor at $\phi = 0$ through the flux insertion argument in the Sec. IV A. As a result, the chiral combinations of the two d -wave components in the two intravalley pairings are restricted to be the same and this intravalley PDW order is also degenerate with a intervalley uniform d -wave pairing. The second kind of chiral d -wave PDW is favored as the unique order of the ground state, if the initial values of the intravalley scatterings g_{1i} are larger than intervalley scatterings g_{2i} , as is shown in Fig. 6. Different from the first kind of PDW order, the chiral combinations of the two d -wave components in the two intravalley pairings can be the same or different but related by a time-reversal symmetry, which means that one intravalley pairing picks $d_1 + id_2$ and the other intravalley pairing picks $d_1 - id_2$. We first take the same chiral combinations in the two intravalley pairings to investigate the mean field spectrum and then investigate the different topological properties of both kinds of chiral combinations. The mean field Hamiltonian of this chiral PDW order whose center of mass momenta are $\pm\mathbf{K}$ for the \pm valleys,

respectively, is

$$\begin{aligned}\hat{H}_{\text{MF}} &= \hat{H}_0 + \hat{H}_{\text{pairing}}, \\ \hat{H}_0 &= -t \sum_{i, \hat{a}_j} \sum_{v=\pm, \sigma} e^{iv\pi/3} \hat{c}_{v, \sigma}^\dagger(i) \hat{c}_{v, \sigma}(i + \hat{a}_j) + \text{H.c.}, \\ \hat{H}_{\text{pairing}} &= \Delta \sum_{k, v=\pm} [d_1(k) + id_2(k)] \hat{c}_{\sigma, v}^\dagger(k + v\mathbf{K}) i\sigma_y \hat{c}_{\sigma', v}^\dagger(-k) \\ &\quad + \text{H.c.},\end{aligned}\quad (23)$$

where \hat{H}_0 is the tight-binding term as in Eq. (1) with $t' = 0$ and $\phi = \pi/3$. The two d -wave form factors are

$$\begin{aligned}d_1(k) &= -\sqrt{\frac{2}{3}} \left[\cos k_x - 1/2 \cos \left(1/2k_x + \frac{\sqrt{3}}{2}k_y \right) \right. \\ &\quad \left. - 1/2 \cos \left(1/2k_x - \frac{\sqrt{3}}{2}k_y \right) \right], \\ d_2(k) &= -2 \sin \frac{k_x}{2} \sin \frac{\sqrt{3}k_y}{2}.\end{aligned}\quad (24)$$

It can be directly verified that $d_1(k)$ and $d_2(k)$ give the two d -wave PDW eigenvectors in Eq. (13) when the momenta of the operators are taken at the Van Hove singularities.

The spectrum of the Bogoliubov quasiparticles can be exactly obtained as: $E_v(\vec{k}) = \sqrt{(\epsilon_v(\vec{k}) - \mu)^2 + \Delta^2 d_1^2(\vec{k} - v\mathbf{K}) + \Delta^2 d_2^2(\vec{k} - v\mathbf{K})}$, where $v = \pm$ denotes the two valleys, $\epsilon_v(\vec{k}) = -2t \sum_j \cos(\vec{k} \cdot \mathbf{a}_j + v\pi/3)$ is the dispersion of the free fermions, and \mathbf{a}_j are the three nearest neighbor unit vectors on the triangular lattice. The chemical potential μ is set to make the electrons at Van Hove filling. The Bogoliubov quasiparticles are fully gapped with an infinitesimal PDW order parameter Δ , as is shown in Fig. 7.

Since the quasiparticle of each valley is fully gapped with a PDW order parameter, we can investigate the Chern number of each valley. The Chern number is defined as

$$\mathcal{N}_v = \frac{1}{4\pi} \int_{\text{BZ}} d\mathbf{k} [\hat{\mathbf{h}} \cdot (\partial_{k_x} \hat{\mathbf{h}} \times \partial_{k_y} \hat{\mathbf{h}})], \quad (25)$$

where $\hat{\mathbf{h}} = (\Re[\Delta(\mathbf{k})], \Im[\Delta(\mathbf{k})], \epsilon_v(\vec{k}) - \mu)/E_v(\vec{k})$ and $\Re[\Delta(\mathbf{k})] = \Delta d_1(\vec{k} - v\mathbf{K})$, $\Im[\Delta(\mathbf{k})] = \Delta d_2(\vec{k} - v\mathbf{K})$. The valley Chern number \mathcal{N}_v is just the winding numbers defined by the number of times that the superconducting phase of $\Delta(\vec{k})$ slips 2π when \mathbf{k} sweeps around the Fermi surface [81]. Since there are two pockets on the Fermi surface of each valley, the Chern number \mathcal{N}_v of both valleys is equal to 4 if the two chiral combinations of the two d -wave components in the two intravalley pairings are the same, and \mathcal{N}_\pm equals ± 4 if the chiral combinations in the two intravalley pairings are $d_1 + id_2$ and $d_1 - id_2$, respectively. In both cases, there are eight chiral Majorana edge modes or equivalently four chiral complex fermion edge modes per valley [81–84].

The degeneracy between opposite valleys can be lifted by a valley splitting field, which is experimentally realizable through a tiny magnetic field if the valley g factor is larger than the spin g factor, e.g., in the ABC trilayer graphene with a hexagonal boron nitride substrate [51]. This valley polarized PDW always hosts a quantized thermal hall effect with the

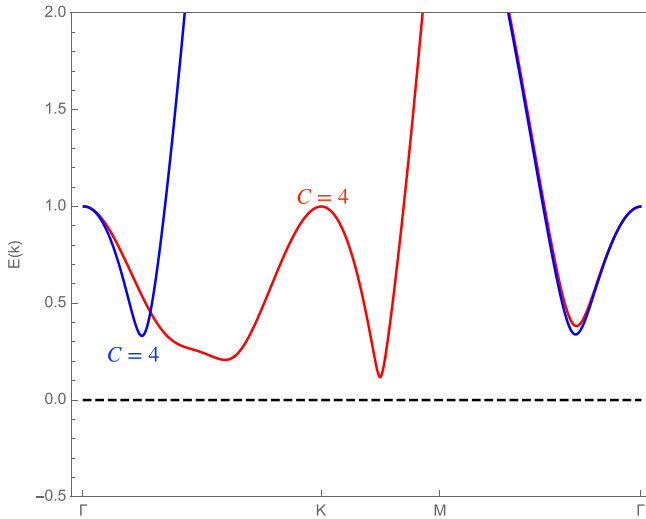


FIG. 7. The energy spectrum of Bogoliubov quasiparticles of the chiral d -wave pair-density-wave mean field. The order parameter amplitude Δ can be obtained from the divergent energy scale y_c as is mentioned in the caption of Fig. 6 and we take here $\Delta = 0.3t$ as a representative value. The red line and blue line represent the spectrum of the quasiparticles in the \pm valleys. Each valley is fully gapped with a PDW order and contributes a Chern number $\mathcal{N} = 4$.

quantized thermal hall conductance $k_{xy} = \frac{4\pi^2 k_B^2 T}{3h}$. More interestingly, the resulting valley polarized PDW has additional novel transport phenomena such as superconducting diode effect [85–87] and nonreciprocal Josephson effect [88]. In the superconducting diode effect, the critical superconducting currents parallel or antiparallel to the center of mass pairing momentum are different due to the broken inversion and time-reversal symmetry. This critical current difference can also be obtained through our mean-field Hamiltonian, similar to the calculation in the FF state [86], but this detailed calculation is beyond the scope of this paper and we leave it for future work.

V. HIGHER ORDER VAN HOVE SINGULARITIES: TWO PATCH MODEL

The band structure from Eq. (1) also hosts two higher order Van Hove singularities located at $\pm\mathbf{K} = \pm(\frac{4\pi}{3}, 0)$, if the condition $\sin(\pi/6 - \phi) = 3t'/t$ is satisfied. For $t' = 0$, this happens when $\phi = \pi/6$. For a small but nonzero t' , this happens when ϕ is slightly below (above) $\pi/6$ for $t' > 0$ (< 0). The Fermi surface at this higher-order Van Hove doping is illustrated in Fig. 8, which shows that a finite t' breaks the perfect nesting. This can also be seen from the energy dispersion near these two HOVHS:

$$\begin{aligned}\epsilon_1(\mathbf{k}) &= \kappa_1(k_x^3 - 3k_x k_y^2) - \kappa_2(k_x^2 + k_y^2)^2 + \mu \\ &= \kappa_1 k^3 \cos 3\theta - \kappa_2 k^4 + \mu, \\ \epsilon_2(\mathbf{k}) &= -\kappa_1(k_x^3 - 3k_x k_y^2) - \kappa_2(k_x^2 + k_y^2)^2 + \mu \\ &= -\kappa_1 k^3 \cos 3\theta - \kappa_2 k^4 + \mu,\end{aligned}\quad (26)$$

where $\kappa_1 = \sqrt{t^2 - 9t'^2}/4$, $\kappa_2 = 9t'/16$ and we have introduced k and θ such that $k_x = k \cos \theta$ and $k_y = k \sin \theta$. Note

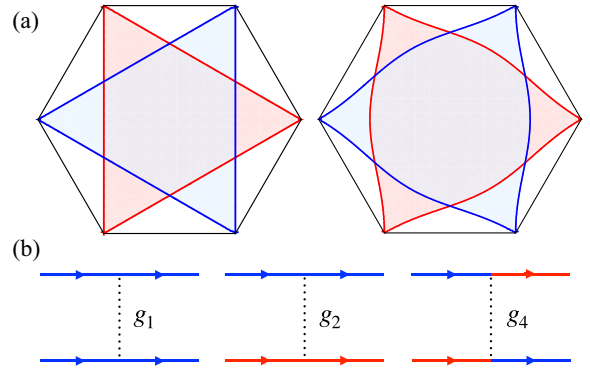


FIG. 8. (a) Fermi surface at higher-order Van Hove doping with $t' = 0$ (left) and $-0.1t$ (right). The red and blue colors represent the two valleys with opposite flux. (b) The symmetry allowed four fermion interaction in the $SU(N_f)(N_f \geq 2)$ two patch model. Since the two patches are centered at $\pm\mathbf{K}$, there is no umklapp interaction.

that if $t' = 0$ and $\mu = 0$, only the cubic terms in these dispersions are present, and this corresponds to the perfect nesting case where $\epsilon_1(\mathbf{k}) = -\epsilon_2(\mathbf{k})$. A finite t' is associated with the k^4 term and hence spoils the FS nesting. A nonzero μ also has the effect of nesting breaking. As we shall see below, the effect of t' is to diminish the divergence of the bare susceptibilities in different channels. t' and μ serve as tuning parameters in our model.

If we take two patches near the two Van Hove singularities near $\pm\mathbf{K}$, the density of states $\nu(E)$ of each patch are the same and diverge polynomially as $\nu(E) \approx E^{-\frac{1}{3}}$. The detailed calculations of $\nu(E)$ are listed in the Appendix. The divergence of the DOS near $\pm\mathbf{K}$ legitimizes our two patch approximation, in which we consider fermions only near these two points, and apply pRG to investigate the competing electronic orders. In the following, we first discuss the building blocks (i.e., the bare susceptibilities) for our pRG analysis, and then we analyze the RG equations and identify the leading instability in various cases.

A. Bare susceptibilities

In the two patch model, Fermi surface nesting occurs with a nesting vector $\mathbf{Q} = 2\mathbf{K}$ if t' and μ are negligible. The nesting would result in a \ln divergence for the particle-hole susceptibility which competes with superconductivity. However, because of the power-law divergence of the DOS in the presence of HOVHS, the logarithmic divergence is less important here: the particle-hole instabilities compete with superconductivity in any case, regardless of the nesting effect.

More interestingly, the HOVHS located at $\pm\mathbf{K}$ are not time-reversal symmetric points and are dubbed as type-II HOVHS, in contrast to the type-I HOVHS where the dispersion has a form such as $ak_y^2 - bk_x^4$ [89,90]. One remarkable feature of the type-II HOVHS is that, besides the divergent susceptibilities in particle-particle channel at zero momentum and particle-hole channel at \mathbf{Q} , those in particle-particle channel at \mathbf{Q} and in particle-hole channel at zero momentum also diverge in similar manner. In other words, the four channels are comparable in the low-energy limit and one has to treat all of them on equal footing. This leads to a competition among

the uniform superconductivity, the finite momentum pairing with center of mass momentum \mathbf{Q} , the charge and spin density wave with momentum \mathbf{Q} , the ferromagnetic instability (FM) and the charge Pomeranchuk instability (PI). The PI is a Fermi surface instability which spontaneously breaks the point symmetry group of the underlying lattice and thus the ground state possesses nonzero angular momentum [91–93].

Consequently, we need the following four bare susceptibilities as our RG building blocks:

$$\begin{aligned}\Pi_{pp}(0) &= \int \frac{d^2\mathbf{k}}{(2\pi)^2} \frac{1 - n_F[\epsilon_1(\mathbf{k})] - n_F[\epsilon_2(-\mathbf{k})]}{\epsilon_1(\mathbf{k}) + \epsilon_2(-\mathbf{k})}, \\ \Pi_{pp}(\mathbf{Q}) &= \int \frac{d^2\mathbf{k}}{(2\pi)^2} \frac{1 - n_F[\epsilon_1(\mathbf{k})] - n_F[\epsilon_1(-\mathbf{k})]}{\epsilon_1(\mathbf{k}) + \epsilon_1(-\mathbf{k})}, \\ \Pi_{ph}(\mathbf{Q}) &= - \int \frac{d^2\mathbf{k}}{(2\pi)^2} \frac{n_F[\epsilon_1(\mathbf{k})] - n_F[\epsilon_2(\mathbf{k})]}{\epsilon_1(\mathbf{k}) - \epsilon_2(\mathbf{k})}, \\ \Pi_{ph}(0) &= - \int \frac{d^2\mathbf{k}}{(2\pi)^2} \frac{\partial n_F(\epsilon)}{\partial \epsilon} \\ &= \int \frac{d^2\mathbf{k}}{(2\pi)^2} \frac{\beta}{4 \cosh^2[\beta\epsilon_1(\mathbf{k})/2]},\end{aligned}\quad (27)$$

where $\epsilon_1(\mathbf{k})$ and $\epsilon_2(\mathbf{k})$ are given in Eq. (26). In the special case when $t' = 0$ and $\mu = 0$, one can make use of $\int d^2\mathbf{k}/(2\pi)^2 = \int dE\nu(E)$ to obtain the low-energy behavior of Eq. (27), where the concrete expression of the DOS $\nu(E)$ is listed in the Appendix. After evaluating the factors numerically we have

$$\begin{aligned}\Pi_{pp}(0) = \Pi_{ph}(\mathbf{Q}) &\approx 0.527 \frac{t^{-2/3}}{T^{1/3}}, \\ \Pi_{pp}(\mathbf{Q}) = \Pi_{ph}(0) &\approx 0.177 \frac{t^{-2/3}}{T^{1/3}}.\end{aligned}\quad (28)$$

If $\mu \neq 0$, the above scaling behaviors still hold (but with different numerical factors) when T is much larger than μ . However, if μ becomes the largest, these bare susceptibilities no longer have a power-law divergence with T . Instead, it is easy to see in this case

$$\begin{aligned}\Pi_{pp}(0) &\sim \frac{1}{|\mu|^{1/3}} \ln \frac{\Lambda}{T}, \\ \Pi_{pp}(\mathbf{Q}), \Pi_{ph}(0), \Pi_{ph}(\mathbf{Q}) &\sim \frac{1}{|\mu|^{1/3}}.\end{aligned}\quad (29)$$

Thus, in low-temperature limit with a finite μ , only the uniform SC channel has the potential instability. Below we will disregard this case, by assuming we are in the limit $T \gg |\mu|$ such that the scaling behaviors in Eq. (28) persist to the lowest T of our interest.

For $t' \neq 0$, it's rather difficult to obtain a relation as simple as Eq. (28), but a direct numerical calculation from Eq. (27) is feasible. In Fig. 9, we plot the numerical results of the four bare susceptibilities as a function of T with $t' = 0.01t$ and $0.2t$ in the upper and lower panels, respectively. For comparison, the result in Eq. (28) at $t' = 0$ is plotted as the dashed and dotted lines. In both cases, all the four bare susceptibilities scale as $1/T^{1/3}$ when T becomes small enough. We clearly see that the finite t' has little effect on the small T behavior of $\Pi_{pp}(0)$, while it reduces the prefactor in $\Pi_{ph}(\mathbf{Q})$ significantly and enhances $\Pi_{pp}(\mathbf{Q})$ and $\Pi_{ph}(0)$ slightly. As

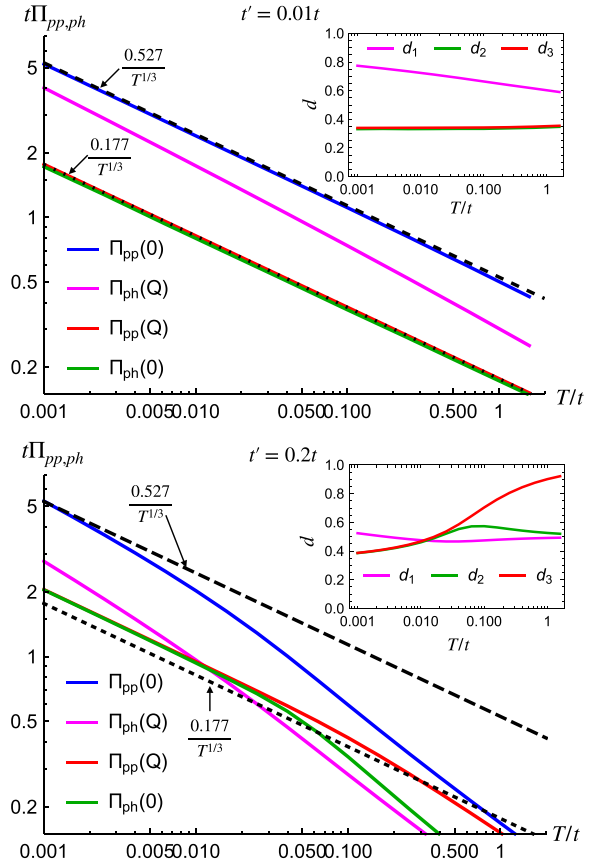


FIG. 9. Various susceptibilities near the higher-order Van Hove filling as a function of temperature T , obtained using $t' = 0.01t$ (top) and $0.2t$ (bottom) (t' is the next-nearest neighbor hopping) and in the limit $T \gg |\mu|$. The insets show temperature dependence of the nesting parameters $d_1 = \Pi_{ph}(\mathbf{Q})/\Pi_{pp}(0)$, $d_2 = \Pi_{ph}(0)/\Pi_{pp}(0)$, and $d_3 = \Pi_{pp}(\mathbf{Q})/\Pi_{pp}(0)$, where $\Pi_{ph}(\mathbf{Q})$, $\Pi_{pp}(\mathbf{Q})$ are the bare susceptibilities with momentum \mathbf{Q} in the particle-hole and particle-particle channel respectively and $\Pi_{ph}(0)$, $\Pi_{pp}(0)$ are the bare susceptibility with zero momentum in the particle-hole and particle-particle channel respectively. For comparison we also show $\Pi_{pp}(0)$ and $\Pi_{pp}(\mathbf{Q})$ at $t' = \mu = 0$ as the dashed and dotted lines.

a result, $\Pi_{ph}(\mathbf{Q})$, once identical to $\Pi_{pp}(0)$ when $t' = 0$ [see Eq. (28)], now becomes smaller. In the insets of Fig. 9, we show the temperature dependence of the nesting parameters, defined as $d_1 = \Pi_{ph}(\mathbf{Q})/\Pi_{pp}(0)$, $d_2 = \Pi_{ph}(0)/\Pi_{pp}(0)$ and $d_3 = \Pi_{pp}(\mathbf{Q})/\Pi_{pp}(0)$. In the ideal case when $t' = 0$, we have $d_1 = 1$ and $d_2 = d_3 = 0.336 \approx 1/3$. With a nonzero t' , all these parameters becomes T -dependent, but have weak T dependence in $T \rightarrow 0$ limit. Moreover, we now have d_1 significantly reduced, while $d_2 \approx d_3$ almost intact. These results legitimize our following RG analysis, in which we take all the three nesting parameters as constant in low- T limit.

B. The phase diagram from RG analysis

There are four symmetry allowed four fermion interactions in the two patch model here, as is shown in Fig. 8(b). The parquet RG analysis here parallels the above RG analysis of the six patch model with conventional Van Hove singularities. As a result, we leave the detailed RG equations and vertex

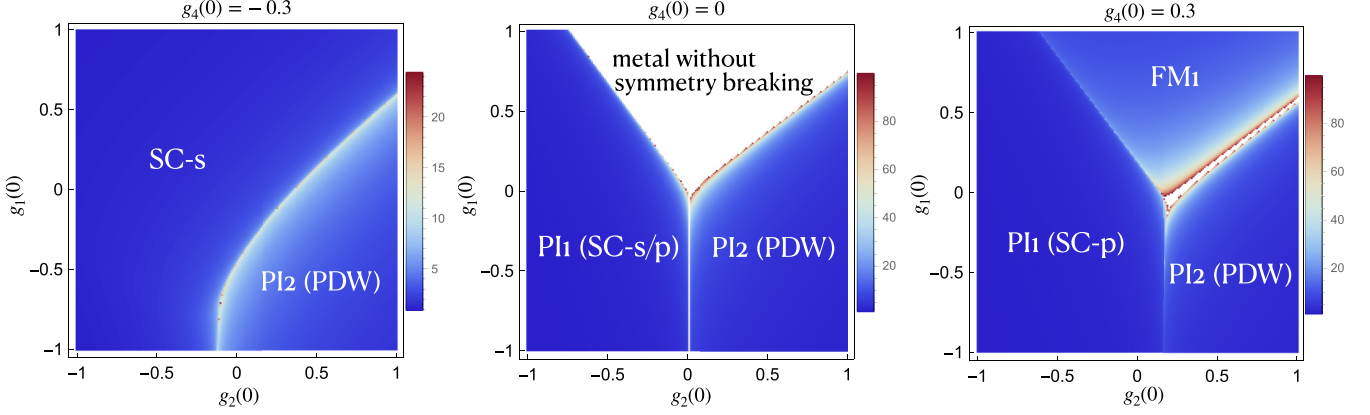


FIG. 10. Phase diagram in the two patch HOVHS case for different initial values of g_1 , g_2 and g_4 . Again all the interactions are measured in units of t . The RG equation is solved with $t' = 0.2t$, $\mu = 0$. The leading orders are marked, while those inside the parenthesis are subleading. The PI1 and PI2 in the figures stand for the Pomeranchuk instability in the s -wave and p -wave channels, respectively.

equations in the Appendix and only summarize the resulting phase diagram here. We want to mention that there are two kinds of FM and PI vertices respectively, which we label as FM_1 , PI_1 and FM_2 , PI_2 . FM_1 , PI_1 are the s -wave ferromagnetic order and Pomeranchuk order respectively, which preserve sign when changing patches,¹ while FM_2 and PI_2 are in the p -wave channel and change sign on these two patches.

We first look into the case of perfect nesting, where $d_1 = 1$ and $d_2 = d_3 = 1/3$. Under this condition, the leading instability of the ground state are three degenerate orders: charge density wave, spin density wave and PI_2 . The PDW order parameter is the subleading instability.

Further, a finite next-nearest neighbor hopping t' gives a richer phase diagram. In Fig. 10, we present the phase diagram for the two patch model with $t' = 0.2t$, obtained from various initial interactions. These phase diagrams are shown in the plane of $g_1(0)$ - $g_2(0)$, and we choose three different $g_4(0)$ from the left panel to the right panel of Fig. 10, which correspond to $g_4(0) = -0.3, 0, 0.3$ respectively. Firstly, if $g_4(0) = 0$, g_4 stays zero under the RG flow. In this case, depending on whether $g_2(0)$ is repulsive or attractive, the leading instabilities are Δ_{PI_2} and Δ_{PI_1} , respectively. We also note that for repulsive g_2 , the subleading order is PDW, while for attractive g_2 , the subleading order is degenerate s - and p -wave uniform SC. If $g_1(0)$ becomes large and $g_2(0)$ stays small, both g_1 and g_2 flows to zero, for which there is no onset of instability. We term this case as metal without symmetry breaking. Similar behavior has been found in a model with a single HOVHS in the weak coupling regime in Ref. [94], which names the gapless metallic state as the “supermetal,” and also in the same two patch model but with $N_f = 1$ instead [35,74]. Whether the ground state is interacting or noninteracting can be justified by the Wilsonian RG which includes the competition between tree level and one loop contribution.

¹The ground state with s -wave (charge)Pomeranchuk order is also defined as “trivial gapped,” since the ground state breaks no lattice symmetries and is not degenerate. Here we define it as the s -wave (charge) Pomeranchuk order just to condense the notation.

Secondly, if we start from a repulsive initial $g_4(0) > 0$, the charge Pomeranchuk instabilities PI_1 and PI_2 are stable with respect to this perturbation. What’s more, the degeneracy between the subleading s -wave and p -wave SC when $g_4 = 0$ is lifted by the nonzero g_4 . And the p -wave SC wins over the s -wave SC with a repulsive $g_4(0) > 0$. In the metal phase regime when $g_4(0) = 0$, we now have FM_1 as the leading order. Near the boundary between FM_1 and PI_2 orders, the critical value y_c is progressively larger than in other areas, which means the boundary between FM_1 and PI_2 is still a gapless metal without symmetry breaking. Finally, if we start from an attractive $g_4(0) < 0$, we have another fixed point where the s -wave uniform SC becomes the leading order (see the left panel in Fig. 10).

In all cases, the PDW phase is subleading, which indicates a strong tendency of the long-range ordering of PDW. We close this section by noticing that, PDW can be the leading order once we introduce an valley Zeeman term splitting term in the system [51]. For example, one can differentiate the phase factor ϕ in Eq. (1) for different valleys by setting $\phi_+ \neq \phi_-$. This valley Zeeman breaks the time-reversal symmetry between \mathbf{K} and $-\mathbf{K}$, and as a result the two HOVHS do not show up at the same energy. Then we effectively obtain a one-patch model, located either around \mathbf{K} or $-\mathbf{K}$. The interpatch interactions g_2 and g_4 are therefore absent. The only allowed interaction is g_1 , governed by the RG equation

$$\dot{g}_1 = [(3 - N_f)d - 1]g_1^2, \quad (30)$$

where we use $\Pi_{pp}(\mathbf{Q})$ as the running parameter and $d = \Pi_{ph}(0)/\Pi_{pp}(\mathbf{Q})$. Once g_1 flows to strong attraction and $d < 1$, the leading order is then a valley polarized PDW.

VI. DISCUSSION AND CONCLUSION

In this work, we analyzed, based on an unbiased weak coupling RG approach, various competing orders of two models with different types of Van Hove singularities. In the first case, the system hosts six different conventional Van Hove singularities where the DOS diverges logarithmically. In the other case, we discuss a system with two type-II higher order Van Hove singularities where the DOS diverges in a power-law manner.

In both cases, the bare PDW susceptibilities are enhanced to the same order of the most divergent bare BCS susceptibility, and thus becomes one of many competing orders including the uniform SC and density waves in particle-hole channel. We find that, with certain initial interactions and nesting parameters, the PDW order wins over all other orders and becomes the leading instability.

We argue the both cases considered here can be realized in moiré systems such as twisted bilayer graphene, twisted double bilayer graphene and twisted bilayer TMD, for which the CVHS and HOVHS can be achieved by tuning moiré band structure through an applied out-of-plane displacement field. Another crucial ingredient for realizing the PDW order is the necessity of keeping both spin and valley degrees of freedom. This can be seen by comparing the $N_f = 1$ and $N_f = 2$ models. In the former case, the system becomes effectively spinless with a nonzero ϕ . Then the number of symmetry allowed interactions is reduced. For example, in the two patch spinless model at higher-order Van Hove filling, only g_2 is allowed. As a result, the PDW ground state cannot be realized in the $N_f = 1$ two patch model [35,74]. Keeping both spin and valley degrees of freedom results in an SU(4) symmetry at $\phi = 0$. Pairing at this case can be classified based how the spin and valley form doublet as we discussed in Sec. III. We also discussed the local transformation that connects the order parameters at $\phi = 0$ and those at $\phi = \pi/3$. From the view of the local transformation, we argued that only the valley triplet pairing at $\phi = 0$ can be mapped into the PDW order at $\phi = \pi/3$. We find that the pairing symmetry must be either s -wave or d -wave. In the d -wave situation, the ground state is most likely to be a $d + id$ configuration in order to be fully gaped. It will be interesting to further investigate this chiral PDW phase.

The PDW order obtained in the six patch case has finite momentum $\pm\mathbf{K}$. However we note this is different from the unidirectional PDW, which has both \mathbf{Q} and $-\mathbf{Q}$ pairing and the spatial configuration is a stripe SC. Here the momentum is associated with valley index such that the PDW is like Fulde-Ferrell state for each valley. Since the FS of each valley has only one nesting vector in the particle-particle channel, a natural way to arrive at the LO state is to add a small coupling between different valleys. However, we find that a small valley coupling also changes the pairing momentum in the six patch model, such that the PDW becomes incommensurate.

In the six patch case, the degeneracy between different valleys can be lifted by including some valley splitting field, giving rise to valley polarized PDW. In the two patch case, such valley splitting field is necessary for realizing the PDW order. In both cases, we obtain a valley polarized PDW. Although this PDW order does not have spatial nodal lines, it has other interesting properties such as superconducting diode effect [85–87], in which the critical current is nonreciprocal, i.e., it is larger in one direction but smaller in the opposite direction. Other interesting effect such as dc-Josephson effect has also been discussed when this PDW order develops [88].

Finally, we notice it is possible to realize some exotic orders through partial melting of the chiral PDW found in this paper. These include, chiral nematic order $(\Delta_1(\mathbf{K}) + i\Delta_2(\mathbf{K}))(\Delta_1^*(\mathbf{K}) + i\Delta_2^*(\mathbf{K}))$ which breaks lattice rotation and time-reversal symmetry, charge- $4e$ PDW $(\Delta_1(\mathbf{K}) +$

$i\Delta_2(\mathbf{K}))(\Delta_1(\mathbf{K}) - i\Delta_2(\mathbf{K}))$, and even chiral charge- $6e$ uniform SC $(\Delta_1(\mathbf{K}) + i\Delta_2(\mathbf{K}))^3$. Identifying the instabilities towards these orders and revealing about their physical properties require additional work which we leave for future studies.

ACKNOWLEDGMENTS

We thank Hong Yao, Sri Raghu, Mengxing Ye, and in particular Andrey Chubukov for useful discussions. Y.-M.W. is grateful to the support of Shuimu Fellow Foundation at Tsinghua University. F.W. is supported by National Natural Science Foundation of China (Grant No. 12274333), National Key Research and Development Program of China (Grant No. 2021YFA1401300), and start-up funding of Wuhan University.

APPENDIX A: CALCULATIONS OF THE BARE SUSCEPTIBILITIES IN THE SIX PATCH CASE

The dispersion near the six conventional Van Hove singularities are

$$\begin{aligned}\epsilon_1(\vec{k}) &= \epsilon_1(\vec{k}) = -1/2(t + 9t_1)k_x^2 + \frac{3}{2}(t + t_1)k_y^2, \\ \epsilon_{2,3}(\vec{k}) &= \epsilon_{2,3}(\vec{k}) = tk_x^2 - 3t_1k_y^2 \pm \sqrt{3}(t + t_1)k_xk_y.\end{aligned}\quad (\text{A1})$$

We start from the simple case with perfect nested Fermi surface ($t' = 0$). We introduce two parameters: $a_{\pm} = \sqrt{\frac{t}{2}}(k_x \pm \sqrt{3}k_y)$, and the dispersion in Eq. (A1) can be rewritten as $\epsilon_1(\vec{k}) = -a_+a_-$, $\epsilon_{2,3}(\vec{k}) = a_{\pm}(a_+ + a_-)$. And the bare susceptibilities are

$$\begin{aligned}\Pi_{ph}(\mathbf{Q}_{\pm}, T) &= -hT \sum_n \int_{-\sqrt{\Lambda}}^{\sqrt{\Lambda}} \frac{da_+ da_-}{(i\omega_n - a_+ a_-)[i\omega_n + a_+(a_+ + a_-)]}, \\ \Pi_{pp}(0, T) &= \Pi_{pp}(\pm\mathbf{K}, T) \\ &= -hT \sum_n \int_{-\sqrt{\Lambda}}^{\sqrt{\Lambda}} \frac{da_+ da_-}{(i\omega_n + a_+ a_-)(i\omega_n - a_+ a_-)},\end{aligned}\quad (\text{A2})$$

where Λ is the UV energy cutoff. We note the expressions in Eq. (A2) have been evaluated in Ref. [33], and the results are

$$\begin{aligned}\Pi_{pp}(0, T) &= \Pi_{pp}(\pm\mathbf{K}, T) = \frac{1}{4\sqrt{3}\pi^2 t} \ln^2 \frac{\Lambda}{T}, \\ \Pi_{ph}(\mathbf{Q}_{\pm}, T) &= \frac{1}{8\sqrt{3}\pi^2 t} \ln^2 \frac{\Lambda}{T}.\end{aligned}\quad (\text{A3})$$

When a finite next-nearest-neighbor hopping t' or/and chemical potential is introduced, all the log divergence will be replaced by $\ln \frac{\Lambda}{\max\{T, \mu, t'\}}$ except the Cooper logarithm in $\Pi_{pp}(0, T)$ and $\Pi_{pp}(\pm\mathbf{K}, T)$ [30,31].

APPENDIX B: PROJECTION OF THE LATTICE INTERACTION

In this section, we project the lattice interaction in Eq. (2) to g_{ij} of the six patch model. The lattice interaction consists

the Hubbard interaction, spin Hund interaction, orbital Hund interaction and Heisenberg interaction. The Hubbard interaction gives the same initial values for all the g_{1i} and g_{2i} . We start from the spin Hund interaction:

$$\begin{aligned} V_h \sum_i (c_i^\dagger \vec{S} c_i)^2 &= V_h \sum_{i,\alpha,\beta,a,b} [2c_{i,\alpha,a}^\dagger c_{i,\beta,a} c_{i,\beta,b}^\dagger c_{i,\alpha,b} - n_i^2] \\ &= -V_h \sum_{i,a,b} [2c_{i,a}^\dagger c_{i,b} c_{i,b}^\dagger c_{i,a} + n_i^2], \end{aligned} \quad (\text{B1})$$

where α, β are the spin indices, a, b are the valley indices and the spin summation is implied in the last line. We have also neglected the quadratic term of fermion operators going from the first line to the second line, which is just the chemical potential. The spin Hund coupling gives the initial values of g_{ij} as $g_{1i} = -3V_h$, $g_{2i} = -V_h$, $g_{4i} = -2V_h$.

Similarly, the projection of orbital Hund interaction to the low-energy g_{ij} interactions is

$$\begin{aligned} K \sum_i (c_i^\dagger \vec{L} c_i)^2 &= K \sum_{i,\alpha,\beta,a,b} [(c_{i,+}^\dagger + c_{i,-}^\dagger + c_{i,-}^\dagger c_{i,+})^2 \\ &\quad - (c_{i,+}^\dagger c_{i,-} - c_{i,-}^\dagger c_{i,+})^2 \\ &\quad + (c_{i,+}^\dagger c_{i,+} - c_{i,-}^\dagger c_{i,-})^2] \\ &= K \sum_i [2c_{i,+}^\dagger c_{i,+} c_{i,-}^\dagger c_{i,+} \\ &\quad + 2c_{i,-}^\dagger c_{i,-} c_{i,+}^\dagger c_{i,-} \\ &\quad + (c_{i,+}^\dagger c_{i,+} - c_{i,-}^\dagger c_{i,-})^2], \end{aligned} \quad (\text{B2})$$

which give the initial values of g_{ij} as: $g_{1i} = K$, $g_{2i} = -K$, $g_{4i} = 2K$.

Finally, the Heisenberg interaction consists three parts: the nearest-neighbour spin Hund coupling, orbital Hund coupling and spin-orbital Hund coupling:

$$\begin{aligned} J \sum_{\langle ij \rangle, n} c_i^\dagger T^n c_i c_j^\dagger T^n c_j \\ = J \sum_{\langle ij \rangle} (c_i^\dagger \vec{\sigma} c_i)(c_j^\dagger \vec{\sigma} c_j) + J \sum_{\langle ij \rangle} (c_i^\dagger \vec{\tau} c_i)(c_j^\dagger \vec{\tau} c_j) \\ + J \sum_{\langle ij \rangle} [c_i^\dagger \vec{\tau} \otimes \vec{\sigma} c_i][c_j^\dagger \vec{\tau} \otimes \vec{\sigma} c_j]. \end{aligned} \quad (\text{B3})$$

We project each part of the Heisenberg interaction to the low-energy degrees of freedom separately. We start from the simplest nearest-neighbor orbital Hund coupling which does not flip the spin explicitly:

$$\begin{aligned} J \sum_{\langle ij \rangle} (c_i^\dagger \vec{\tau} c_i)(c_j^\dagger \vec{\tau} c_j) \\ = J \sum_{\langle ij \rangle} (2c_{i,+}^\dagger c_{i,-} c_{j,-}^\dagger c_{j,+} + 2c_{i,-}^\dagger c_{i,+} c_{j,+}^\dagger c_{j,-} \\ + c_{i,+}^\dagger c_{i,+} c_{j,+}^\dagger c_{j,+} + c_{i,-}^\dagger c_{i,-} c_{j,-}^\dagger c_{j,-} \\ - c_{i,+}^\dagger c_{i,+} c_{j,-}^\dagger c_{j,-} - c_{i,-}^\dagger c_{i,-} c_{j,+}^\dagger c_{j,+}). \end{aligned} \quad (\text{B4})$$

g_{ij} acquire anisotropic initial values from this term as

$$\begin{aligned} g_{11} = g_{12} = J, \quad g_{13} = g_{14} = J \sum_{\hat{a}_i} \cos(\mathbf{Q}_+ \cdot \hat{a}_i) = -J, \\ g_{21} = g_{22} = -J, \quad g_{23} = g_{24} = -J \sum_{\hat{a}_i} \cos(\mathbf{Q}_+ \cdot \hat{a}_i) = J, \\ g_{41} = g_{44} = 2J \sum_{\hat{a}_i} \cos(\mathbf{K} \cdot \hat{a}_i) = -3J, \\ g_{42} = g_{43} = 2J \sum_{\hat{a}_i} \cos(\mathbf{Q}_- \cdot \hat{a}_i) = J. \end{aligned} \quad (\text{B5})$$

Next we consider the spin Hund coupling, to which we apply the SU(2) Fierz identity to bring it into the spin preserving form:

$$\begin{aligned} J \sum_{\langle ij \rangle} (c_i^\dagger \vec{S} c_i)(c_j^\dagger \vec{S} c_j) \\ = J \sum_{i,\alpha,\beta,a,b} (2c_{i,\alpha,a}^\dagger c_{i,\beta,a} c_{j,\beta,b}^\dagger c_{j,\alpha,b} - n_i n_j) \\ = -J \sum_{\langle ij \rangle} (2c_{i,+}^\dagger c_{j,+} c_{j,+}^\dagger c_{i,+} + 2c_{i,-}^\dagger c_{j,-} c_{j,-}^\dagger c_{i,-} \\ + 2c_{i,+}^\dagger c_{j,-} c_{j,-}^\dagger c_{i,+} + 2c_{i,-}^\dagger c_{j,+} c_{j,+}^\dagger c_{i,-} + n_i n_j), \end{aligned} \quad (\text{B6})$$

g_{ij} acquire the following initial values from this term as

$$\begin{aligned} g_{11} = -3J, \quad g_{12} = -2J \sum_{\hat{a}_i} \cos(\mathbf{Q}_+ \cdot \hat{a}_i) - J = J, \\ g_{13} = -3J \sum_{\hat{a}_i} \cos(\mathbf{Q}_+ \cdot \hat{a}_i) = 3J, \\ g_{14} = -2J - J \sum_{\hat{a}_i} \cos(\mathbf{Q}_+ \cdot \hat{a}_i) = -J, \\ g_{21} = g_{22} = -J, \quad g_{23} = g_{24} = -J \sum_{\hat{a}_i} \cos(\mathbf{Q}_+ \cdot \hat{a}_i) = J, \\ g_{41} = g_{42} = -2J, \quad g_{43} = g_{44} = -2J \sum_{\hat{a}_i} \cos(\mathbf{Q}_+ \cdot \hat{a}_i) = 2J. \end{aligned} \quad (\text{B7})$$

Finally, the projection of the spin-orbital Hund coupling is

$$\begin{aligned} J \sum_{\langle ij \rangle} [c_i^\dagger \vec{\tau} \otimes \vec{\sigma} c_i][c_j^\dagger \vec{\tau} \otimes \vec{\sigma} c_j] \\ = J [2c_{i,+}^\dagger \vec{\sigma} c_{i,-} c_{j,-}^\dagger \vec{\sigma} c_{j,+} + 2c_{i,-}^\dagger \vec{\sigma} c_{i,+} c_{j,+}^\dagger \vec{\sigma} c_{j,-} \\ + (c_{i,+}^\dagger \vec{\sigma} c_{i,+}) \cdot (c_{j,+}^\dagger \vec{\sigma} c_{j,+}) + (c_{i,-}^\dagger \vec{\sigma} c_{i,-}) \cdot (c_{j,-}^\dagger \vec{\sigma} c_{j,-}) \\ - (c_{i,+}^\dagger \vec{\sigma} c_{i,+}) \cdot (c_{j,-}^\dagger \vec{\sigma} c_{j,-}) - (c_{i,-}^\dagger \vec{\sigma} c_{i,-}) \cdot (c_{j,+}^\dagger \vec{\sigma} c_{j,+})] \\ = J \sum_{\langle ij \rangle} (-4c_{i,+}^\dagger c_{j,+} c_{j,-}^\dagger c_{i,-} - 2c_{i,+}^\dagger c_{i,-} c_{j,-}^\dagger c_{j,+} \\ - 2c_{i,+}^\dagger c_{j,+} c_{j,+}^\dagger c_{i,+} - c_{i,+}^\dagger c_{i,+} c_{j,+}^\dagger c_{j,+} + 2c_{i,+}^\dagger c_{j,-} c_{j,-}^\dagger c_{i,+} \\ + c_{i,+}^\dagger c_{i,+} c_{j,-}^\dagger c_{j,-}) + (+ \leftrightarrow -). \end{aligned} \quad (\text{B8})$$

g_{ij} acquire the following initial values from this term as

$$\begin{aligned}
 g_{11} &= -2J - J = -3J, & g_{12} &= -2J \sum_{\hat{a}_i} \cos(\mathbf{Q}_+ \cdot \hat{a}_i) - J = J, \\
 g_{13} &= -2J \sum_{\hat{a}_i} \cos(\mathbf{Q}_+ \cdot \hat{a}_i) - J \sum_{\hat{a}_i} \cos(\mathbf{Q}_+ \cdot \hat{a}_i) = 3J, \\
 g_{14} &= -2J - J \sum_{\hat{a}_i} \cos(\mathbf{Q}_+ \cdot \hat{a}_i) = -J, \\
 g_{21} &= -4J \sum_{\hat{a}_i} \cos(\mathbf{K} \cdot \hat{a}_i) + J = 7J, \\
 g_{22} &= -4J \sum_{\hat{a}_i} \cos(\mathbf{Q}_- \cdot \hat{a}_i) + J = -J, \\
 g_{23} &= -4J \sum_{\hat{a}_i} \cos(\mathbf{Q}_- \cdot \hat{a}_i) + J \sum_{\hat{a}_i} \cos(\mathbf{Q}_+ \cdot \hat{a}_i) = -3J, \\
 g_{24} &= -4J \sum_{\hat{a}_i} \cos(\mathbf{K} \cdot \hat{a}_i) + J \sum_{\hat{a}_i} \cos(\mathbf{Q}_+ \cdot \hat{a}_i) = 5J, \\
 g_{41} &= 2J - 2J \sum_{\hat{a}_i} \cos(\mathbf{K} \cdot \hat{a}_i) = 5J, \\
 g_{42} &= 2J - 2J \sum_{\hat{a}_i} \cos(\mathbf{Q}_- \cdot \hat{a}_i) = J, \\
 g_{43} &= 2J \sum_{\hat{a}_i} \cos(\mathbf{Q}_+ \cdot \hat{a}_i) - 2J \sum_{\hat{a}_i} \cos(\mathbf{Q}_- \cdot \hat{a}_i) = -3J, \\
 g_{44} &= 2J \sum_{\hat{a}_i} \cos(\mathbf{Q}_+ \cdot \hat{a}_i) - 2J \sum_{\hat{a}_i} \cos(\mathbf{K} \cdot \hat{a}_i) = J.
 \end{aligned} \tag{B9}$$

The total contribution of the Heisenberg interaction to the initial values of g_{ij} are

$$\begin{aligned}
 g_{11} &= -5J, & g_{12} &= 3J, & g_{13} &= 5J, & g_{14} &= -3J, \\
 g_{21} &= 5J, & g_{22} &= -3J, & g_{23} &= -J, & g_{24} &= 7J, \\
 g_{4i} &= 0.
 \end{aligned} \tag{B10}$$

APPENDIX C: DENSITY OF STATES OF THE TWO PATCH MODEL

Given the dispersions of the two patch model in Eq. (26), the density of states near these two HOVHS can be obtained via $\nu_{1,2}(E) = \sum_{\mathbf{k}} \delta(E - \epsilon_{1,2}(\mathbf{k}))$. Since $\epsilon_1(\mathbf{k}) = \epsilon_2(-\mathbf{k})$, $\nu_1(E)$ and $\nu_2(E)$ are in fact identical therefore we omit the subscript. The explicit expression of $\nu(E)$ is

$$\begin{aligned}
 \nu(E) &= \int \frac{kd\mathbf{k}d\theta}{(2\pi)^2} \delta(E - \kappa_1 k^3 \cos 3\theta + \kappa_2 k^4 - \mu) \\
 &= \frac{2}{(2\pi)^2} \int_0^\infty \frac{dk}{|E'|} \text{Re} \left[\frac{k}{\sqrt{\kappa_1^2 k^6 / E'^2 - (1 + \kappa_2 k^4 / E')^2}} \right],
 \end{aligned} \tag{C1}$$

where $E' = E - \mu$. For the case when $t' = 0$ and hence $\kappa_2 = 0$, the above integral can be evaluated and the result is

$$\begin{aligned}
 \nu(E)|_{t'=0} &= \frac{1}{|E - \mu|^{1/3}} \frac{2\kappa_1^{-2/3}}{(2\pi)^2} \int_1^\infty dx \frac{x}{\sqrt{x^6 - 1}} \\
 &= \frac{\nu_0}{|E - \mu|^{1/3}},
 \end{aligned} \tag{C2}$$

where $\nu_0 = \kappa_1^{-2/3} \Gamma(7/6) / (2\Gamma(2/3)\pi^{3/2}) \approx 0.155t^{-2/3}$, which is identical to that given in Ref. [35]. With a nonzero t' , we have

$$\begin{aligned}
 \nu(E) &= \frac{\kappa_1^{-2/3}}{|E'|^{1/3}} \frac{2}{(2\pi)^2} \\
 &\times \int_0^\infty dx \text{Re} \frac{x}{\sqrt{x^6 - (1 - x^4 |E'|^{1/3} \kappa_2 / \kappa_1^{4/3})^2}}.
 \end{aligned} \tag{C3}$$

Since we are interested in low-energy fermions in the vicinity near $\pm\mathbf{K}$, we can make E' small, and the leading divergent term in the above equation is the same with Eq. (C2). Therefore we anticipate that even for the nonperfect nesting case, $\nu(E)$ also have a power-law divergence.

The divergence of the DOS near $\pm\mathbf{K}$ legitimizes our two patch approximation, in which we consider fermions only near these two points, and apply pRG to investigate the competing electronic orders. In the following, we first discuss the building blocks (i.e., the bare susceptibilities) for our pRG analysis, and then we analyze the RG equations and identify the leading instability in various cases.

APPENDIX D: RENORMALIZATION GROUP ANALYSIS OF THE TWO PATCH MODEL

As in the six patch model, here we also consider the system with spin SU(2) symmetry. Unlike the six patch model, the symmetry allowed interactions are much fewer. Figure 8(b) shows all the three interactions. Note there is no umklapp interaction.

The one-loop RG equations for these interactions can be obtained in a similar way as in the six patch model, but here the running parameter $y = \Pi_{pp}(0)$ scales as $1/T^{1/3}$ instead of $\ln^2 T$. The results are

$$\begin{aligned}
 \dot{g}_1 &= [(3 - N_f)d_2 - d_3]g_1^2 - N_f d_2 g_2^2 + d_2 g_4^2 + 2d_2 g_2 g_4, \\
 \dot{g}_2 &= (d_1 - 1)g_2^2 - g_4^2 + 2d_2 g_1 g_4 + (2 - 2N_f)d_2 g_1 g_2, \\
 \dot{g}_4 &= 2(d_1 - 1)g_2 g_4 + 2d_2 g_1 g_4 - N_f d_1 g_4^2,
 \end{aligned} \tag{D1}$$

where N_f is the number of fermion flavors for each valley component. We take $N_f = 2$ in our following discussion. The nesting parameters d_i at the low-energy limit are approximated by constant values and defined via $d_1 = \Pi_{ph}(\mathbf{Q})/y$, $d_2 = \Pi_{ph}(0)/y$ and $d_3 = \Pi_{pp}(\mathbf{Q})/y$. This is justified by the numerical results plotted in Fig. 9. Similar to the six patch model analysis, the interactions g_i can also flow to some strong coupling fixed point at some critical value y_c . We thus can assume the scaling form $g_i = G_i/(y_c - y)$ near y_c and then confirm it. Because of the fewer interactions in the two patch case, competing orders are also fewer. We consider PDW, uniform SC, CDW, SDW, ferromagnetism (FM), and

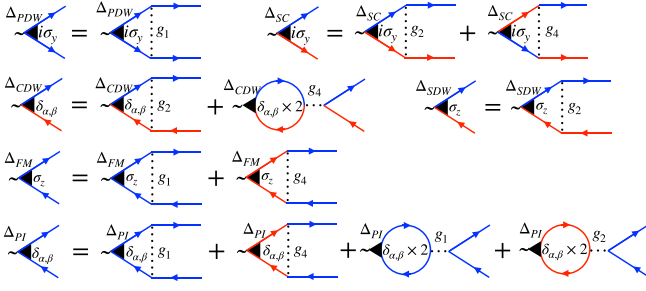


FIG. 11. Diagrammatic representation of the one-loop RG equations for various order parameters in the two patch case. See the Fig. 8 for the color convention. PI here stands for the Pomeranchuk instability, which breaks the point group symmetry of the lattice.

charge Pomeranchuk instability (PI). We list all the possible order parameters and their RG equations diagrammatically in Fig. 11. The corresponding RG equations for these orders are explicitly given by

$$\begin{aligned}\dot{\Delta}_{PDW} &= -d_3 g_1 \Delta_{PDW}, \\ \dot{\Delta}_{SC}^s &= -(g_2 + g_4) \Delta_{SC}^s, \quad \dot{\Delta}_{SC}^p = -(g_2 - g_4) \Delta_{SC}^p, \\ \dot{\Delta}_{CDW} &= d_1 (g_2 - 2g_4) \Delta_{CDW}, \\ \dot{\Delta}_{SDW} &= d_1 g_2 \Delta_{SDW}, \\ \dot{\Delta}_{FM1} &= d_2 (g_1 + g_4) \Delta_{FM},\end{aligned}$$

$$\begin{aligned}\dot{\Delta}_{FM2} &= d_2 (g_1 - g_4) \Delta_{FM}, \\ \dot{\Delta}_{PI1} &= d_2 (-g_1 - 2g_2 + g_4) \Delta_{PI1}, \\ \dot{\Delta}_{PI2} &= d_2 (-g_1 + 2g_2 - g_4) \Delta_{PI2}.\end{aligned}\quad (D2)$$

Here the s -wave SC order parameter has the same sign at both patches, while the p -wave order parameter changes sign between patches. Similarly, Δ_{FM1} and Δ_{PI1} are the vertices of the s -wave ferromagnetic order and Pomeranchuk order respectively, which preserve sign when changing patches, while Δ_{FM2} and Δ_{PI2} are in the p -wave channel and change sign on these two patches.

The possible order is associated with a divergent susceptibility, for which the behavior close to y_c can also be expressed as $\chi \sim (y_c - y)^\alpha$ with $\alpha < 0$. Like in the six patch model, we can determine α from the RG equations for χ , and the resulting α is given in terms of G_i , i.e., the same as Eq. (22).

We first look into the case of perfect nesting, where $d_1 = 1$ and $d_2 = d_3 = 1/3$. Under this condition, the RG equation has a fixed point at $G_1 = -G_2 < 0$ and $G_4 = 0$. This fixed point indicates a degenerate ground state among Δ_{CDW} , Δ_{SDW} , and Δ_{PI2} . This can be directly seen from Eq. (D2): the flow equation for these three orders are the same if g_4 vanishes. The PDW order parameter is the subleading one, due to the fact that $d_3 < d_1$ and $g_1 \rightarrow -\infty$. However it cannot be ordered upon decreasing T because the corresponding $\alpha_{PDW} > 0$. The phase diagram with a nonzero t' has been discussed in the maintext.

APPENDIX E: THE STABILITY OF THE FIXED POINT

The asymptotic behavior of strong coupling fixed points in the one-loop RG equations are $g_{ij} \approx \frac{G_{ij}}{y_c - y}$, $i = 1, 2$ and $j = 1, 2, 3, 4$. The stability of fixed trajectories toward strong coupling is analyzed through the stability matrices of the ratios of coupling constants, or ‘‘rays’’ [33,77,95,96]. Since the interaction g_{12} and g_{22} generally flow to $+\infty$, as we can see from the RG equations of the six patch model. We can use either of them as a new running parameter and define the rays as $x_{ij} = g_{ij}/g_{12}$ or $x_{ij} = g_{ij}/g_{22}$.

We take a typical nesting parameter $d = 1/2$. The g_{22} interaction flows to $+\infty$ in the strong coupling fix point which favor the chiral d -wave PDW, and we use g_{22} as the new flow parameter to analyze the stability of this ray. The fixed point ratios are The RG equations can be cast into

$$\begin{aligned}\frac{dx_{11}}{d \ln g_{22}} &= -x_{11} - \frac{x_{11}^2 + 2x_{13}^2}{d(1 + x_{23}^2)}, \quad \frac{dx_{12}}{d \ln g_{22}} = -x_{12} + \frac{x_{12}^2 + x_{13}^2 + x_{43}^2 + x_{44}^2}{1 + x_{23}^2}, \\ \frac{dx_{13}}{d \ln g_{22}} &= -x_{13} - \frac{2x_{11}x_{13} + x_{13}^2}{d(1 + x_{23}^2)} + 2 \times \frac{2x_{12}x_{13} - 2x_{23}x_{24} + x_{23}x_{44} + x_{24}x_{43} + x_{43}x_{44} - x_{13}x_{14}}{1 + x_{23}^2}, \\ \frac{dx_{14}}{d \ln g_{22}} &= -x_{14} + 2 \times \frac{x_{12}x_{14} + x_{24}x_{44} + x_{23}x_{43} - x_{24}^2 - x_{14}^2 - x_{23}^2}{1 + x_{23}^2}, \\ \frac{dx_{21}}{d \ln g_{22}} &= -x_{21} - \frac{x_{21}^2 + 2x_{23}^2 + x_{41}^2 + 2x_{43}^2}{d(1 + x_{23}^2)}, \\ \frac{dx_{23}}{d \ln g_{22}} &= -x_{23} + \frac{-2x_{21}x_{23} - x_{23}^2 + 2d(x_{23} + x_{12}x_{23} - 2x_{23}x_{14} - x_{13}x_{24})}{d(1 + x_{23}^2)} + \frac{-2x_{41}x_{43} - x_{43}^2 + 2d(x_{13}x_{44} + x_{14}x_{43})}{d(1 + x_{23}^2)}, \\ \frac{dx_{24}}{d \ln g_{22}} &= -x_{24} + 2 \frac{x_{12}x_{24} + x_{14}x_{44} + x_{13}x_{43} - x_{13}x_{23} - 2x_{14}x_{24}}{1 + x_{23}^2}, \\ \frac{dx_{41}}{d \ln g_{22}} &= -x_{41} - 2 \frac{x_{21}x_{41} + 2x_{23}x_{43}}{d(1 + x_{23}^2)}, \quad \frac{dx_{42}}{d \ln g_{22}} = -x_{42} + 2 \frac{x_{42} + x_{23}x_{43} - x_{43}^2 - x_{42}^2}{1 + x_{23}^2},\end{aligned}$$

$$\begin{aligned}\frac{dx_{43}}{d \ln g_{22}} &= -x_{43} - 2 \frac{x_{21}x_{43} + x_{23}x_{41} + x_{23}x_{43}}{d(1+x_{23}^2)} + 2 \frac{x_{12}x_{43} + x_{13}x_{44} + x_{43} + x_{23}x_{42} - 2x_{42}x_{43}}{1+x_{23}^2}, \\ \frac{dx_{44}}{d \ln g_{22}} &= -x_{44} + 2 \frac{x_{12}x_{44} + x_{13}x_{43}}{1+x_{23}^2}.\end{aligned}\quad (\text{E1})$$

Similar equations can also be obtained if we choose g_{12} as the new flow parameter. For convenience we use the eleven component vector \vec{x} to compactly label the eleven ratios on the right hand side of Eq. (E1), and use $f_i(\vec{x})$, $i = 1, 2, 3, \dots, 7$ to label the expressions on the left hand side of Eq. (E1). Then we do small perturbations to the stable ray, which is equivalent to linearize Eq. (E1) around the stable ray:

$$\left. \frac{d\delta x_i}{d \ln g_{22}} = \frac{\partial f_i(\vec{x})}{\partial x_j} \right|_{\vec{x}=\vec{x}^*} \delta x_j = M_{ij} \delta x_j. \quad (\text{E2})$$

If the stability matrix $M_{ij} = \partial f_i(\rho_1, \rho_4)/\partial \rho_j$ has eigenvalues which are all negative, then the fixed point is stable. Otherwise it has positive eigenvalue(s), then the fixed point is not stable. We have testified that for the PDW and uniform SC orders, all the eigenvalues of their corresponding stability matrix are negative.

In the two patch model, similar analysis can be applied. For example, when the interactions flow to a fixed point at which $g_1 \rightarrow -\infty$, we can introduce $\ln |g_1|$ as a new running parameter around the fixed point to see if this is stable. Defining $x_2 = -g_2/g_1$ and $x_4 = -g_4/g_1$, the RG equations for g_2 and g_4 can be cast into

$$\begin{aligned}\frac{dx_2}{d \ln |g_1|} &= -x_2 - \frac{(d_1 - 1)x_2^2 - x_4^2 - 2d_2x_4 - (2 - 2N_f)d_2x_2}{[(3 - N_f)d_2 - d_3] - N_f d_2 x_2^2 + d_2 x_4^2 + 2d_2 x_2 x_4}, \\ \frac{dx_4}{d \ln |g_1|} &= -x_4 - \frac{2(d_1 - 1)x_2 x_4 - 2d_2 x_4 - N_f d_1 x_4^2}{[(3 - N_f)d_2 - d_3] - N_f d_2 x_2^2 + d_2 x_4^2 + 2d_2 x_2 x_4}.\end{aligned}\quad (\text{E3})$$

Again we can define the corresponding stability matrix, and we find that all the leading orders shown in Fig. 10 are stable.

-
- [1] D. F. Agterberg, J. S. Davis, S. D. Edkins, E. Fradkin, D. J. Van Harlingen, S. A. Kivelson, P. A. Lee, L. Radzihovsky, J. M. Tranquada, and Y. Wang, The physics of pair-density waves: Cuprate superconductors and beyond, *Annu. Rev. Condens. Matter Phys.* **11**, 231 (2020).
- [2] P. Fulde and R. A. Ferrell, Superconductivity in a strong spin-exchange field, *Phys. Rev.* **135**, A550 (1964).
- [3] A. I. Larkin and Y. N. Ovchinnikov, Nonuniform state of superconductors, *Sov. Phys. JETP* **20**, 762 (1965).
- [4] C. C. Agosta, Inhomogeneous superconductivity in organic and related superconductors, *Crystals* **8**, 285 (2018).
- [5] Y. Matsuda and H. Shimahara, Fulde-ferrell-larkin-ovchinnikov state in heavy fermion superconductors, *J. Phys. Soc. Jpn.* **76**, 051005 (2007).
- [6] A. Gurevich, Upper critical field and the fulde-ferrel-larkin-ovchinnikov transition in multiband superconductors, *Phys. Rev. B* **82**, 184504 (2010).
- [7] C.-w. Cho, J. H. Yang, N. F. Q. Yuan, J. Shen, T. Wolf, and R. Lortz, Thermodynamic Evidence for the Fulde-Ferrell-Larkin-Ovchinnikov State in the KFe_2As_2 Superconductor, *Phys. Rev. Lett.* **119**, 217002 (2017).
- [8] E. Berg, E. Fradkin, E.-A. Kim, S. A. Kivelson, V. Oganesyan, J. M. Tranquada, and S. C. Zhang, Dynamical Layer Decoupling in a Stripe-Ordered High- T_c Superconductor, *Phys. Rev. Lett.* **99**, 127003 (2007).
- [9] Y. Wang, D. F. Agterberg, and A. Chubukov, Coexistence of Charge-Density-Wave and Pair-Density-Wave Orders in Underdoped Cuprates, *Phys. Rev. Lett.* **114**, 197001 (2015).
- [10] Y. Wang, D. F. Agterberg, and A. Chubukov, Interplay between pair- and charge-density-wave orders in underdoped cuprates, *Phys. Rev. B* **91**, 115103 (2015).
- [11] Y. Wang, S. D. Edkins, M. H. Hamidian, J. C. S. Davis, E. Fradkin, and S. A. Kivelson, Pair density waves in superconducting vortex halos, *Phys. Rev. B* **97**, 174510 (2018).
- [12] J. M. Tranquada, B. J. Sternlieb, J. D. Axe, Y. Nakamura, and S. Uchida, Evidence for stripe correlations of spins and holes in copper oxide superconductors, *Nature* **375**, 561 (1995).
- [13] M. Fujita, H. Goka, K. Yamada, J. M. Tranquada, and L. P. Regnault, Stripe order, depinning, and fluctuations in $\text{La}_{1.875}\text{Ba}_{0.125}\text{CuO}_4$ and $\text{La}_{1.875}\text{Ba}_{0.075}\text{Sr}_{0.050}\text{CuO}_4$, *Phys. Rev. B* **70**, 104517 (2004).
- [14] M. Hückler, M. v. Zimmermann, G. D. Gu, Z. J. Xu, J. S. Wen, G. Xu, H. J. Kang, A. Zheludev, and J. M. Tranquada, Stripe order in superconducting $\text{La}_{2-x}\text{Ba}_x\text{CuO}_4$ ($0.095 \leq x \leq 0.155$), *Phys. Rev. B* **83**, 104506 (2011).
- [15] E. Berg, E. Fradkin, S. A. Kivelson, and J. M. Tranquada, Striped superconductors: how spin, charge and superconducting orders intertwine in the cuprates, *New J. Phys.* **11**, 115004 (2009).
- [16] P. A. Lee, Amperean Pairing and the Pseudogap Phase of Cuprate Superconductors, *Phys. Rev. X* **4**, 031017 (2014).
- [17] D. F. Agterberg and H. Tsunetsugu, Dislocations and vortices in pair-density-wave superconductors, *Nat. Phys.* **4**, 639 (2008).
- [18] L. Nie, G. Tarjus, and S. A. Kivelson, Quenched disorder and vestigial nematicity in the pseudogap regime of the cuprates, *Proc. Natl. Acad. Sci. USA* **111**, 7980 (2014).

- [19] E. Fradkin, S. A. Kivelson, and J. M. Tranquada, Colloquium: Theory of intertwined orders in high temperature superconductors, *Rev. Mod. Phys.* **87**, 457 (2015).
- [20] E. Berg, E. Fradkin, and S. A. Kivelson, Charge-4e superconductivity from pair-density-wave order in certain high-temperature superconductors, *Nat. Phys.* **5**, 830 (2009).
- [21] D. F. Agterberg, M. Geracie, and H. Tsunetsugu, Conventional and charge-six superfluids from melting hexagonal fuldefferell-larkin-ovchinnikov phases in two dimensions, *Phys. Rev. B* **84**, 014513 (2011).
- [22] J. Ge, P. Wang, Y. Xing, Q. Yin, H. Lei, Z. Wang, and J. Wang, Discovery of charge-4e and charge-6e superconductivity in kagome superconductor csv3sb5 , [arXiv:2201.10352](https://arxiv.org/abs/2201.10352).
- [23] G. Li, A. Luican, J. M. B. Lopes dos Santos, A. H. Castro Neto, A. Reina, J. Kong, and E. Y. Andrei, Observation of Van Hove singularities in twisted graphene layers, *Nat. Phys.* **6**, 109 (2010).
- [24] I. Brihuega, P. Mallet, H. González-Herrero, G. Trambly de Laissardière, M. M. Ugeda, L. Magaud, J. M. Gómez-Rodríguez, F. Ynduráin, and J.-Y. Veullen, Unraveling the Intrinsic and Robust Nature of Van Hove Singularities in Twisted Bilayer Graphene by Scanning Tunneling Microscopy and Theoretical Analysis, *Phys. Rev. Lett.* **109**, 196802 (2012).
- [25] S. Wu, Z. Zhang, K. Watanabe, T. Taniguchi, and E. Y. Andrei, Chern insulators, Van Hove singularities and topological flat bands in magic-angle twisted bilayer graphene, *Nat. Mater.* **20**, 488 (2021).
- [26] N. F. Q. Yuan, H. Isobe, and L. Fu, Magic of high-order Van Hove singularity, *Nat. Commun.* **10**, 5769 (2019).
- [27] F. Wu and S. Das Sarma, Ferromagnetism and superconductivity in twisted double bilayer graphene, *Phys. Rev. B* **101**, 155149 (2020).
- [28] D. Guerci, P. Simon, and C. Mora, Higher-order Van Hove singularity in magic-angle twisted trilayer graphene, *Phys. Rev. Res.* **4**, L012013 (2022).
- [29] Y.-P. Lin and R. M. Nandkishore, Parquet renormalization group analysis of weak-coupling instabilities with multiple high-order Van Hove points inside the Brillouin zone, *Phys. Rev. B* **102**, 245122 (2020).
- [30] N. Furukawa, T. M. Rice, and M. Salmhofer, Truncation of a Two-Dimensional Fermi Surface due to Quasiparticle Gap Formation at the Saddle Points, *Phys. Rev. Lett.* **81**, 3195 (1998).
- [31] R. Nandkishore, L. S. Levitov, and A. V. Chubukov, Chiral superconductivity from repulsive interactions in doped graphene, *Nat. Phys.* **8**, 158 (2012).
- [32] H. Isobe, N. F. Q. Yuan, and L. Fu, Unconventional Superconductivity and Density Waves in Twisted Bilayer Graphene, *Phys. Rev. X* **8**, 041041 (2018).
- [33] Y.-P. Lin and R. M. Nandkishore, Chiral twist on the high- T_c phase diagram in moiré heterostructures, *Phys. Rev. B* **100**, 085136 (2019).
- [34] Y.-T. Hsu, F. Wu, and S. Das Sarma, Topological superconductivity, ferromagnetism, and valley-polarized phases in moiré systems: Renormalization group analysis for twisted double bilayer graphene, *Phys. Rev. B* **102**, 085103 (2020).
- [35] Y.-T. Hsu, F. Wu, and S. Das Sarma, Spin-valley locked instabilities in moiré transition metal dichalcogenides with conventional and higher-order Van Hove singularities, *Phys. Rev. B* **104**, 195134 (2021).
- [36] D. Shaffer, J. Wang, and L. H. Santos, Unconventional self-similar hofstadter superconductivity from repulsive interactions *Nat. Commun.* **13**, 7785 (2022).
- [37] D.-C. Lu, T. Wang, S. Chatterjee, and Y.-Z. You, Correlated metals and unconventional superconductivity in rhombohedral trilayer graphene: A renormalization group analysis, *Phys. Rev. B* **106**, 155115 (2022).
- [38] F. Wu, T. Lovorn, E. Tutuc, and A. H. MacDonald, Hubbard Model Physics in Transition Metal Dichalcogenide Moiré Bands, *Phys. Rev. Lett.* **121**, 026402 (2018).
- [39] F. Wu, T. Lovorn, E. Tutuc, I. Martin, and A. H. MacDonald, Topological Insulators in Twisted Transition Metal Dichalcogenide Homobilayers, *Phys. Rev. Lett.* **122**, 086402 (2019).
- [40] Z. Zhang, Y. Wang, K. Watanabe, T. Taniguchi, K. Ueno, E. Tutuc, and B. J. LeRoy, Flat bands in twisted bilayer transition metal dichalcogenides, *Nat. Phys.* **16**, 1093 (2020).
- [41] S. Shabani, D. Halbertal, W. Wu, M. Chen, S. Liu, J. Hone, W. Yao, D. N. Basov, X. Zhu, and A. N. Pasupathy, Deep moiré potentials in twisted transition metal dichalcogenide bilayers, *Nat. Phys.* **17**, 720 (2021).
- [42] A. Weston, Y. Zou, V. Enaldiev, A. Summerfield, N. Clark, V. Zólyomi, A. Graham, C. Yelgel, S. Magorrian, M. Zhou, J. Zultak, D. Hopkinson, A. Barinov, T. H. Bointon, A. Kretinin, N. R. Wilson, P. H. Beton, V. I. Fal'ko, S. J. Haigh, and R. Gorbachev, Atomic reconstruction in twisted bilayers of transition metal dichalcogenides, *Nat. Nanotechnol.* **15**, 592 (2020).
- [43] T. Devakul, V. Crépel, Y. Zhang, and L. Fu, Magic in twisted transition metal dichalcogenide bilayers, *Nat. Commun.* **12**, 6730 (2021).
- [44] Y. Zhang, T. Liu, and L. Fu, Electronic structures, charge transfer, and charge order in twisted transition metal dichalcogenide bilayers, *Phys. Rev. B* **103**, 155142 (2021).
- [45] M. Angeli and A. H. MacDonald, Gamma valley transition metal dichalcogenide moiré bands, *Proc. Natl. Acad. Sci.* **118**, e2021826118 (2021).
- [46] K. Tran, J. Choi, and A. Singh, Moiré and beyond in transition metal dichalcogenide twisted bilayers, *2D Mater.* **8**, 022002 (2021).
- [47] V. Vitale, K. Atalar, A. A. Mostofi, and J. Lischner, Flat band properties of twisted transition metal dichalcogenide homo- and heterobilayers of MoS_2 , MoSe_2 , WS_2 and WSe_2 , *2D Mater.* **8**, 045010 (2021).
- [48] Z. Bi and L. Fu, Excitonic density wave and spin-valley superfluid in bilayer transition metal dichalcogenide, *Nat. Commun.* **12**, 642 (2021).
- [49] M. M. Scherer, D. M. Kennes, and L. Classen, Chiral superconductivity with enhanced quantized Hall responses in moiré transition metal dichalcogenides, *npj Quantum Mater.* **7**, 100 (2022).
- [50] C. Schrade and L. Fu, Spin-valley density wave in moiré materials, *Phys. Rev. B* **100**, 035413 (2019).
- [51] Y.-H. Zhang and T. Senthil, Bridging Hubbard model physics and quantum hall physics in trilayer graphene/ h - BN moiré superlattice, *Phys. Rev. B* **99**, 205150 (2019).
- [52] Y.-H. Zhang and D. Mao, Spin liquids and pseudogap metals in the $\text{su}(4)$ Hubbard model in a moiré superlattice, *Phys. Rev. B* **101**, 035122 (2020).

- [53] Y.-H. Zhang, D. Mao, Y. Cao, P. Jarillo-Herrero, and T. Senthil, Nearly flat chern bands in moiré superlattices, *Phys. Rev. B* **99**, 075127 (2019).
- [54] N. R. Chebrolu, B. L. Chittari, and J. Jung, Flat bands in twisted double bilayer graphene, *Phys. Rev. B* **99**, 235417 (2019).
- [55] M. Koshino, Band structure and topological properties of twisted double bilayer graphene, *Phys. Rev. B* **99**, 235406 (2019).
- [56] J. Liu, Z. Ma, J. Gao, and X. Dai, Quantum Valley Hall Effect, Orbital Magnetism, and Anomalous Hall Effect in Twisted Multilayer Graphene Systems, *Phys. Rev. X* **9**, 031021 (2019).
- [57] J. Y. Lee, E. Khalaf, S. Liu, X. Liu, Z. Hao, P. Kim, and A. Vishwanath, Theory of correlated insulating behaviour and spin-triplet superconductivity in twisted double bilayer graphene, *Nat. Commun.* **10**, 5333 (2019).
- [58] F. Haddadi, Q. Wu, A. J. Kruchkov, and O. V. Yazyev, Moiré flat bands in twisted double bilayer graphene, *Nano Lett.* **20**, 2410 (2020).
- [59] M. Koshino, N. F. Q. Yuan, T. Koretsune, M. Ochi, K. Kuroki, and L. Fu, Maximally Localized Wannier Orbitals and the Extended Hubbard Model for Twisted Bilayer Graphene, *Phys. Rev. X* **8**, 031087 (2018).
- [60] N. F. Q. Yuan and L. Fu, Model for the metal-insulator transition in graphene superlattices and beyond, *Phys. Rev. B* **98**, 045103 (2018).
- [61] J. Kang and O. Vafek, Symmetry, Maximally Localized Wannier States, and a Low-Energy Model for Twisted Bilayer Graphene Narrow Bands, *Phys. Rev. X* **8**, 031088 (2018).
- [62] D. V. Chichinadze, L. Classen, Y. Wang, and A. V. Chubukov, SU(4) Symmetry in Twisted Bilayer Graphene: An Itinerant Perspective, *Phys. Rev. Lett.* **128**, 227601 (2022).
- [63] L. Wang, E.-M. Shih, A. Ghiotto, L. Xian, D. A. Rhodes, C. Tan, M. Claassen, D. M. Kennes, Y. Bai, B. Kim, K. Watanabe, T. Taniguchi, X. Zhu, J. Hone, A. Rubio, A. N. Pasupathy, and C. R. Dean, Correlated electronic phases in twisted bilayer transition metal dichalcogenides, *Nat. Mater.* **19**, 861 (2020).
- [64] H. Pan, F. Wu, and S. Das Sarma, Band topology, Hubbard model, Heisenberg model, and Dzyaloshinskii-Moriya interaction in twisted bilayer WSe₂, *Phys. Rev. Res.* **2**, 033087 (2020).
- [65] A. Ghiotto, E.-M. Shih, G. S. S. G. Pereira, D. A. Rhodes, B. Kim, J. Zang, A. J. Millis, K. Watanabe, T. Taniguchi, J. C. Hone, L. Wang, C. R. Dean, and A. N. Pasupathy, Quantum criticality in twisted transition metal dichalcogenides, *Nature* **597**, 345 (2021).
- [66] J. Zang, J. Wang, J. Cano, and A. J. Millis, Hartree-fock study of the moiré Hubbard model for twisted bilayer transition metal dichalcogenides, *Phys. Rev. B* **104**, 075150 (2021).
- [67] I. T. Diatlov, V. V. Sudakov, and K. A. Ter-Martirosian, Asymptotic meson-meson scattering theory, *Sov. Phys. JETP* **5**, 631 (1957).
- [68] J. Sólyom, The fermi gas model of one-dimensional conductors, *Adv. Phys.* **28**, 201 (1979).
- [69] A. T. Zheleznyak, V. M. Yakovenko, and I. E. Dzyaloshinskii, Parquet solution for a flat fermi surface, *Phys. Rev. B* **55**, 3200 (1997).
- [70] A. V. Chubukov, D. V. Efremov, and I. Eremin, Magnetism, superconductivity, and pairing symmetry in iron-based superconductors, *Phys. Rev. B* **78**, 134512 (2008).
- [71] F. D. M. Haldane, Model for a Quantum Hall Effect without Landau Levels: Condensed-Matter Realization of the “Parity Anomaly”, *Phys. Rev. Lett.* **61**, 2015 (1988).
- [72] P. Ramond, *Group Theory: A Physicist’s Survey* (Cambridge University Press, Cambridge, UK, 2010).
- [73] C. Xu and L. Balents, Topological Superconductivity in Twisted Multilayer Graphene, *Phys. Rev. Lett.* **121**, 087001 (2018).
- [74] Y.-M. Wu, Z. Wu, and H. Yao, Pair-density-wave and chiral superconductivity in twisted bilayer transition-metal-dichalcogenides [arXiv:2203.05480](https://arxiv.org/abs/2203.05480).
- [75] L. Classen, C. Honerkamp, and M. M. Scherer, Competing phases of interacting electrons on triangular lattices in moiré heterostructures, *Phys. Rev. B* **99**, 195120 (2019).
- [76] A. V. Chubukov, M. Khodas, and R. M. Fernandes, Magnetism, Superconductivity, and Spontaneous Orbital Order in Iron-Based Superconductors: Which Comes First and Why? *Phys. Rev. X* **6**, 041045 (2016).
- [77] V. Cvetkovic, R. E. Throckmorton, and O. Vafek, Electronic multicriticality in bilayer graphene, *Phys. Rev. B* **86**, 075467 (2012).
- [78] B. Binz, D. Baeriswyl, and B. Douçot, Wilson’s renormalization group applied to 2d lattice electrons in the presence of Van Hove singularities, *Eur. Phys. J. B* **25**, 69 (2002).
- [79] J. W. F. Venderbos, Symmetry analysis of translational symmetry broken density waves: Application to hexagonal lattices in two dimensions, *Phys. Rev. B* **93**, 115107 (2016).
- [80] Y. Gannot, Y.-F. Jiang, and S. A. Kivelson, Hubbard ladders at small u revisited, *Phys. Rev. B* **102**, 115136 (2020).
- [81] A. M. Black-Schaffer and C. Honerkamp, Chiral d -wave superconductivity in doped graphene, *J. Phys.: Condens. Matter* **26**, 423201 (2014).
- [82] M. Sato and Y. Ando, Topological superconductors: a review, *Rep. Prog. Phys.* **80**, 076501 (2017).
- [83] N. Read and D. Green, Paired states of fermions in two dimensions with breaking of parity and time-reversal symmetries and the fractional quantum hall effect, *Phys. Rev. B* **61**, 10267 (2000).
- [84] A. M. Black-Schaffer, Edge Properties and Majorana Fermions in the Proposed Chiral d -Wave Superconducting State of Doped Graphene, *Phys. Rev. Lett.* **109**, 197001 (2012).
- [85] N. F. Q. Yuan and L. Fu, Supercurrent diode effect and finite-momentum superconductors, *Proc. Natl. Acad. Sci.* **119**, e2119548119 (2022).
- [86] A. Daido, Y. Ikeda, and Y. Yanase, Intrinsic Superconducting Diode Effect, *Phys. Rev. Lett.* **128**, 037001 (2022).
- [87] F. Ando, Y. Miyasaka, T. Li, J. Ishizuka, T. Arakawa, Y. Shiota, T. Moriyama, Y. Yanase, and T. Ono, Observation of superconducting diode effect, *Nature* **584**, 373 (2020).
- [88] M. Davydova, S. Prembabu, and L. Fu, Universal josephson diode effect, *Sci. Adv.* **8**, eabo0309 (2022).
- [89] H. Yao and F. Yang, Topological odd-parity superconductivity at type-ii two-dimensional Van Hove singularities, *Phys. Rev. B* **92**, 035132 (2015).
- [90] L. Classen, A. V. Chubukov, C. Honerkamp, and M. M. Scherer, Competing orders at higher-order Van Hove points, *Phys. Rev. B* **102**, 125141 (2020).
- [91] I. I. Pomeranchuk, On the stability of a fermi liquid, *Sov. Phys. JETP* **8**, 361 (1959).
- [92] C. Wu, K. Sun, E. Fradkin, and S.-C. Zhang, Fermi liquid instabilities in the spin channel, *Phys. Rev. B* **75**, 115103 (2007).

- [93] A. V. Chubukov, A. Klein, and D. L. Maslov, Fermi-liquid theory and pomeranchuk instabilities: Fundamentals and new developments, *J. Exp. Theor. Phys.* **127**, 826 (2018).
- [94] H. Isobe and L. Fu, Supermetal, *Phys. Rev. Res.* **1**, 033206 (2019).
- [95] O. Vafek and K. Yang, Many-body instability of coulomb interacting bilayer graphene: Renormalization group approach, *Phys. Rev. B* **81**, 041401(R) (2010).
- [96] O. Vafek, Interacting fermions on the honeycomb bilayer: From weak to strong coupling, *Phys. Rev. B* **82**, 205106 (2010).